J. Fluid Mech. (2013), *vol.* 717, *pp.* 535–575.
doi:10.1017/jfm.2012.595

Hybrid Eulerian–Lagrangian simulations for polymer–turbulence interactions

Takeshi Watanabe† and Toshiyuki Gotoh

Graduate School of Engineering, Department of Scientific and Engineering Simulations, Nagoya Institute of Technology, Gokiso, Showa-ku, Nagoya 466-8555, Japan

(Received 30 March 2012; revised 21 November 2012; accepted 29 November 2012; first published online 1 February 2013)

The effects of polymer additives on decaying isotropic turbulence are numerically investigated using a hybrid approach consisting of Brownian dynamics simulations for an enormous number of dumbbells (of the order of 10 billion, $O(10^{10})$) and direct numerical simulations of turbulence making full use of large-scale parallel computations. Reduction of the energy dissipation rate and modification of the kinetic energy spectrum in the dissipation range scale were observed when the reaction term due to the polymer additives was incorporated into the equation of motion for the solvent fluid. An increase in the polymer concentration or Weissenberg number W_i yielded significant modifications of the turbulence statistics at small scales, such as a suppression of the local energy dissipation fluctuations. A power-law decay of the kinetic energy spectrum $E(k, t) \sim k^{-4.7}$ was observed in the wavenumber range below the Kolmogorov length scale when $W_i = 25$. The generation of intense vortices was suppressed by the polymer additives, consistent with previous studies using the constitutive equations. The field structures of the trace of the polymer stress depended on the intensity of its fluctuation: sheet-like structures were observed for the intermediate intensity region and filamentary structures were observed for the intense region. The results obtained with few polymers and large replicas could approximate those with many polymers and smaller replicas as far as the large-scale statistics were concerned.

Key words: isotropic turbulence, non-Newtonian flows, polymers

1. Introduction

It is well known that small amounts of polymer added to a fluid significantly affect the large-scale flow structures. One famous example is the drag reduction phenomenon in wall-bounded turbulent flows (Lumley 1973; Sreenivasan & White 2000; Proccacia, L'vov & Benzi 2008). The specific nature of polymer solution flow is also observed at low Reynolds numbers, where the velocity field randomly fluctuates in space and time due to the elastic instability. This is the so-called elastic turbulence (Groisman & Steinberg 2000; Burghelea, Segre & Steinberg 2006, 2007; Jun & Steinberg 2009), which is used to enhance mixing in micro-channel devices (Groisman & Steinberg 2001; Burghelea, Segre & Steinberg 2004; Arratia *et al.* 2006). Although many experimental and numerical studies have addressed the above phenomena to clarify the

† Email address for correspondence: watanabe@nitech.ac.jp

role of polymer dynamics in flows, our current understanding remains inadequate due to a poor understanding of the complicated interactions between long-chain polymers and flow dynamics, and the resulting dynamics, which involve a wide range of spatial and temporal scales.

When considering the polymer effect on wall-bounded turbulent flows, it is important to note that the details of the interaction between the fluid motion and polymer dynamics depend on the distance from the wall, which plays a critical role in the mechanisms of turbulent mixing and transport. Because the near-wall region remains within the strong extensional flow caused by the streamwise vortices, the polymers in the buffer layer are highly stretched by this flow, implying that the elongational viscosity significantly increases in this region. The increase in viscosity suppresses turbulent fluctuations and correspondingly increases the buffer layer thickness, leading to drag reduction (Lumley 1973; Sreenivasan & White 2000). Conversely, it is also known that the turbulent behaviour far from the wall is directly affected by polymer additives. In this case, the bare interaction between the polymers and the fluctuating local velocity gradient is a fundamental dynamical process. These direct interactions give rise to strong modifications of the small-scale properties of turbulence, such as strain, enstrophy and particle accelerations statistics (Liberzon *et al.* 2005, 2006; Crawford *et al.* 2008). This also leads to modification of the statistical nature at dissipation-range scales and at inertial-range scales for higher concentrations (McComb, Allan & Greated 1977; van Doorn, White & Sreenivasan 1999; Angelis *et al.* 2005; Ouellette, Xu & Bodenschatz 2009).

It is vital to examine the mesoscale dynamics of an isolated polymer in turbulent flows for deeper insight into the peculiar flow nature of dilute polymer solutions. Previous studies have investigated single-polymer dynamics in simple shear (Celani, Puliafito & Turitsyn 2005*b*; Chertkov *et al.* 2005; Gerashchenko & Steinberg 2006) and random flows (Balkovsky, Fouxon & Lebedev 2000; Chertkov 2000; Thiffeault 2003; Afonso & Vincenzi 2005; Celani, Musacchio & Vincenzi 2005*a*; Gerashchenko, Chevallard & Steinberg 2005; Liu & Steinberg 2010). The coil–stretch transition is an important concept for understanding polymer dynamics in turbulence (De Gennes 1974). For simple shear flow with shear intensity S, the polymer takes a coiled configuration if $S\tau < 1$, where τ is the characteristic relaxation time of the polymer chain. For $S\tau > 1$, the polymer exhibits an extended configuration due to the action of the local flow. Because the direction and amplitude of the local shear in turbulence fluctuates randomly and intermittently in space and time, the polymer will manifest complicated behaviour along the fluid particle trajectories, making it difficult to understand the interactions.

In our previous study, we investigated single polymer chain dynamics in isotropic turbulence in a one-way coupling regime (Watanabe & Gotoh 2010). We found that a coil–stretch transition occurred at the characteristic Weissenberg numbers $W_i = \tau/\tau_K = 3$–4, with τ_K being the Kolmogorov time scale. This suggests that the Lagrangian correlation time of the velocity gradient tensor $\boldsymbol{\nabla u}$ ($\sim 4\tau_K$) is a key quantity in determining whether the polymers were stretched. We also found that the statistical nature of the polymer chain (multi-beads model) was well approximated by the dumbbell model. In addition, the relationship between polymer elongation and local flow topology was investigated by analysing the conditioned statistics of polymer elongation on the invariants of $\boldsymbol{\nabla u}$. To discuss turbulence modification by polymer additives, we must incorporate the reaction force from an enormous number of polymers into the equation of motion for the solvent fluid.

In the past, turbulent dilute polymer solution flow has been investigated extensively using constitutive equations such as the Oldroyd-B or FENE-P models (Bird *et al.* 1987). These are the evolution equations for the tensor field representing the polymer conformation and are constructed using a simple polymer model (Bird *et al.* 1987). The constitutive equations are widely used for numerical studies of turbulent drag reduction (Sureshkumar, Beris & Handler 1997; Eckhardt, Kronjager & Schumacher 2002; Boffetta, Celani & Musacchio 2003; Boffetta, Celani & Mazzino 2005; Gillissen 2008; Tamano *et al.* 2009; Perlekar, Mitra & Pandit 2006, 2010; Cai, Li & Zhang 2010) and elastic turbulence (Berti *et al.* 2008) because of the ease of handling the polymer effects on turbulence with numerical simulations. However, a recent study demonstrated that a resolution condition much more stringent than that of the velocity field is required for adequate computation of the FENE-P equation (Jin & Collins 2007).

Under a hybrid approach, the fluid motion is computed using the Navier–Stokes (NS) equations while the polymer dynamics are determined from molecular or Brownian dynamics simulations with an appropriate polymer model (Doi & Edwards 1986; Bird *et al.* 1987). Several studies of polymer solution flow have used a combination of computational fluid dynamics and particle-based simulations of polymer models with and without reaction to fluid motion (Laso & Ottinger 1993; Stone & Graham 2003; Terrapon *et al.* 2004; Davoudi & Schumacher 2006; Peters & Schumacher 2007; Jin & Collins 2007; Watanabe & Gotoh 2010; Yasuda & Yamamoto 2010). The advantage of the hybrid approach is that we can construct a polymer solution model with a rich variety of mechanical properties by introducing several interacting forces among particles. Moreover, it may be suitable to investigate phenomena for which the Lagrangian view is intrinsic, similar to the diffusion of polymer solutions in a turbulent boundary layer (Elbing *et al.* 2010) or the degradation effects of polymers on turbulence (Choi *et al.* 2002). The disadvantage of this approach is that the computational cost greatly increases as the number of polymers is increased. However, we can neglect the interaction among polymers for dilute solutions, implying that the computational cost for evaluating forces among particles is roughly proportional to the number of polymers. In this case, we can perform efficient simulations for an enormous number of polymers dispersed in turbulence using large-scale parallel computations.

Here, we present the development of a two-way coupled simulation method using the hybrid approach. A Brownian dynamics simulation for the polymer chain model coupled with a direct numerical simulation (DNS) of turbulent flow are performed using large-scale parallel computations. We adopt the dumbbell model to represent the dynamics of a long-chain polymer because it can satisfactorily reproduce the overall results obtained by the chain model (Jin & Collins 2007; Watanabe & Gotoh 2010). To gain a significant reaction from the presence of polymers in the fluid, we need a huge number of dumbbells in the flow domain. In this study, on the order of 10 billion ($O(10^{10})$) dumbbells are dispersed in turbulent flow, and their advections and deformations are strictly tracked during the time evolution of the system. We then examine the degree of modification to the turbulent flow by investigating the concentration and Weissenberg number effects on the fundamental statistics and vortical structures for decaying isotropic turbulence. Because there is no mean shear in isotropic turbulence, it is suitable for investigating the effects of polymers on the bulk turbulence by analysing the interaction between the polymers and local velocity gradient fluctuations. Modification of isotropic turbulence by polymer additives has recently been investigated using the DNS of FENE-P model

(Vaithianathan & Collins 2003; Angelis *et al.* 2005; Perlekar *et al.* 2006, 2010; Cai *et al.* 2010). Comparing the present results with those obtained by the FENE-P model may be useful for assessing the hybrid approach used in this study. Moreover, we examine the validity of the assumption used for constructing the polymer stress field from the dispersed dumbbells.

We begin this paper with a brief description of the model equations used in this study in § 2. The details of the numerical method are provided in § 3. The fundamental nature of decaying isotropic turbulence with polymer additives is described in § 4, along with a brief summary of the statistical quantities examined in this study. The effects of polymer additives on decaying turbulence are quantified by varying the parameters, including the concentration and Weissenberg numbers, in § 5. The polymer effects on coherent structures and the specific nature of the polymer stress field are also discussed. The response of the system to changes in the polymer number with fixed physical conditions is examined in § 6. The important findings obtained in this study are provided in § 7, followed by a summary of our results and conclusions in § 8.

2. Polymer solution model

2.1. *Governing equations*

The dumbbell model is used to represent the dynamics of a polymer dispersed in the flow domain. Each polymer is modelled by two beads of radius a connected by a nonlinear spring (Bird *et al.* 1987). The position vectors of each bead in the nth dumbbell are represented by $\boldsymbol{x}_1^{(n)}(t)$ and $\boldsymbol{x}_2^{(n)}(t)$ with $n = 1, 2, \ldots, N_t$ where N_t is the total number of dumbbells dispersed in the flow domain. Here, we consider the flow in a dilute polymer solution and neglect interactions among dumbbells. In addition, due to its small size, the inertia of beads is also neglected. Thus, the equations of motion for the end-to-end vector $\boldsymbol{R}^{(n)}(t) = \boldsymbol{x}_1^{(n)}(t) - \boldsymbol{x}_2^{(n)}(t)$ and the centre-of-mass vector $\boldsymbol{r}_g^{(n)}(t) = (\boldsymbol{x}_1^{(n)}(t) + \boldsymbol{x}_2^{(n)}(t))/2$ of the nth dumbbell are respectively given by

$$\frac{\mathrm{d}\boldsymbol{R}^{(n)}}{\mathrm{d}t} = \boldsymbol{u}_1^{(n)} - \boldsymbol{u}_2^{(n)} - \frac{1}{2\tau} f\left(\frac{|\boldsymbol{R}^{(n)}|}{L_{max}}\right)\boldsymbol{R}^{(n)} + \frac{r_{eq}}{\sqrt{2\tau}}(\boldsymbol{W}_1^{(n)} - \boldsymbol{W}_2^{(n)}), \tag{2.1}$$

$$\frac{\mathrm{d}\boldsymbol{r}_g^{(n)}}{\mathrm{d}t} = \frac{1}{2}(\boldsymbol{u}_1^{(n)} + \boldsymbol{u}_2^{(n)}) + \frac{r_{eq}}{\sqrt{8\tau}}(\boldsymbol{W}_1^{(n)} + \boldsymbol{W}_2^{(n)}), \quad \boldsymbol{u}_\alpha^{(n)} \equiv \boldsymbol{u}(\boldsymbol{x}_\alpha^{(n)}(t), t), \tag{2.2}$$

where $\boldsymbol{u}(\boldsymbol{x}, t)$ denotes the velocity field of the solvent fluid. We adopt the finitely extensible nonlinear elastic (FENE) model (Bird *et al.* 1987) using

$$f(z) = \frac{1}{1 - z^2} \tag{2.3}$$

for the elastic force of a dumbbell. This dumbbell cannot extend beyond the maximum length L_{max}. The term $\boldsymbol{W}_{1,2}^{(n)}(t)$ indicates a random force representing the Brownian motion of particles in the solvent fluid, which obeys Gaussian statistics with a white-in-time correlation of

$$\langle W_{\alpha,i}^{(n)}(t)\rangle = 0, \tag{2.4}$$

$$\langle W_{\alpha,i}^{(m)}(t) W_{\beta,j}^{(n)}(s)\rangle = \delta_{\alpha\beta}\delta_{ij}\delta_{mn}\delta(t - s), \tag{2.5}$$

where $\langle\cdots\rangle$ denotes the ensemble average, and the subscript variables α, β, i, j, n and m take the values $(\alpha, \beta) = 1$ or 2, $(i, j) = 1$, 2 and 3, and $(n, m) = 1, 2, \ldots, N_t$.

Here δ_{ij} denotes the Kronecker delta and $\delta(t)$ is the Dirac delta function. The constants τ and r_{eq}, defined by

$$\tau = \frac{\zeta}{4k} \tag{2.6}$$

and

$$r_{eq} = \sqrt{\frac{k_B T}{k}}, \tag{2.7}$$

are the relaxation time and the equilibrium length of the dumbbell under $\boldsymbol{u}(\boldsymbol{x}, t) = \boldsymbol{0}$. Here k is the spring constant, $\zeta = 6\pi\nu_s\rho_s a$ (ν_s and ρ_s are, respectively, the kinetic viscosity and the density of the solvent fluid), and k_B and T are the Boltzman constant and temperature, respectively.

The turbulent velocity field obeys the continuity equation for an incompressible fluid

$$\boldsymbol{\nabla} \cdot \boldsymbol{u} = 0, \tag{2.8}$$

and the NS equations

$$\frac{\partial \boldsymbol{u}}{\partial t} + \boldsymbol{u} \cdot \boldsymbol{\nabla}\boldsymbol{u} = -\boldsymbol{\nabla} p + \nu_s \nabla^2 \boldsymbol{u} + \boldsymbol{\nabla} : \boldsymbol{T}^p, \tag{2.9}$$

where $p(\boldsymbol{x}, t)$ is the pressure field. Here, the density of the solvent fluid is set to unity and equal to that of the beads representing the polymer ($\rho_s = \rho_p = 1$) and $\boldsymbol{T}^p(\boldsymbol{x}, t)$ is the polymer stress tensor due to the force acting on the fluid from the dispersed dumbbells. It is defined by

$$T^p_{ij}(\boldsymbol{x}, t) = \frac{\nu_s \eta}{\tau} \left(\frac{L^3_{box}}{N_t} \right) \sum_{n=1}^{N_t} \left[\frac{R^{(n)}_i R^{(n)}_j}{r^2_{eq}} f\left(\frac{|\boldsymbol{R}^{(n)}|}{L_{max}} \right) - \delta_{ij} \right] \delta(\boldsymbol{x} - \boldsymbol{r}^{(n)}_g), \tag{2.10}$$

where $\eta \equiv (3r_{eq}/4a)^2 \Phi_V$ is proportional to the volume fraction of the ensemble of dumbbells $\Phi_V \equiv (8\pi N_t/3)(a/L_{box})^3$. Because η is also represented by the zero shear viscosity ratio of the polymer $\nu_p \equiv \nu_s \eta$ to the solvent viscosity, this is related to the parameter β, which is the ratio of the solvent to the total zero shear rate solution viscosity $\beta \equiv \nu_s/(\nu_s + \nu_p)$, as $\beta = 1/(1 + \eta)$. The derivation of (2.10) is summarized in Appendix.

2.2. *Parameter setting*

In this section, we address how many dumbbells are required to produce a significant turbulence modification. According to an experimental study using polyacrylamide ($M_p = 18 \times 10^6$ a.m.u.), the number of polymers per box with volume l^3_K, where l_K is the Kolmogorov length scale defined by (3.6), can be estimated to be $N_K = 3.6 \times 10^6$ for the case of a $R_\lambda \simeq 50$ and a 5 ppm polymer solution inferred from the data in Ouellette *et al.* (2009). Therefore, the total number of polymers in the computational box is estimated to be $N_t = N_K (L_{box}/l_K)^3 = O(10^{13})$ when the DNS condition ($\Delta x = l_K$) necessary for better convergence of small-scale statistics is applied (Watanabe & Gotoh 2007). The number $N_t = O(10^{13})$ is very large, even when using a state-of-the-art supercomputer. Thus, an approximate method is required to represent the interaction between the fluid motion and polymer dynamics. We propose that N_t can be represented by $N_t = b\tilde{N}_t$, where $\tilde{N}_t$ indicates the total number of dumbbells in computation and b is an artificial parameter representing the number of replicas

per dumbbell. Under this assumption, the polymer stress tensor is approximated by replacing N_t in (2.10) by $\tilde{N}_t$. The effect of the parameter b enters η through the volume fraction Φ_V as $\Phi_V = b(8\pi\tilde{N}_t/3)\,(a/L_{box})^3$. This kind of assumption has been introduced previously for the two-way coupled simulation of a solid-particle suspension in homogeneous turbulence (Bosse, Kleiser & Meiburg 2006) and will be examined in § 6.

The dumbbell parameters r_{eq}, a and L_{max} are determined using experimental parameters under a fixed l_K (Ouellette *et al.* 2009), in which the radius of gyration is $R_g = 0.5$ μm and $L_{max} = 77$ μm for a polyacrylamide polymer solution. We then evaluate $L_{max}/l_K = 0.3$, $r_{eq}/l_K = 3.0 \times 10^{-3}$, and $a/l_K = (3\Phi_V/4\pi N_K)^{1/3} = 7.0 \times 10^{-5}$, where we used the relationship $r_{eq} \simeq \sqrt{2}R_g$ for a Gaussian chain and $l_K \simeq 280$ μm when $R_\lambda = 50$.

The Weissenberg number W_i controls the elastic nature of the polymer model, and is defined by

$$W_i = \frac{\tau}{\tau_K}, \tag{2.11}$$

where the Kolmogorov time scale τ_K is defined by (3.7) using the zero polymer case.

3. Numerical simulations

The DNSs of (2.8) and (2.9) are performed in a periodic box with periodicity $L_{box} = 2\pi$ using the pseudo-spectral method in space and the second-order Runge–Kutta method in time. The number of grid points of the DNSs is set to $N^3 = 128^3$ for all runs except Run F which has a finer spatial resolution ($N^3 = 256^3$). The initial conditions of the velocity field are randomized, obeying Gaussian statistics, with an energy spectrum of

$$E(k,0) = 16\sqrt{\frac{2}{\pi}}\left(\frac{u_0^2}{k_0}\right)\left(\frac{k}{k_0}\right)^4 \exp\left(-2\left(\frac{k}{k_0}\right)^2\right) \quad (u_0 = 1, k_0 = 2), \tag{3.1}$$

as used by Fukayama *et al.* (2000) and Gotoh *et al.* (2007). Here $E(k,t)$ is defined using the Fourier coefficient $\boldsymbol{u}(\boldsymbol{k},t)$ of the Fourier series expansion of $\boldsymbol{u}(\boldsymbol{x},t)$ as

$$E(k,t) \equiv \sum_{\boldsymbol{k}}{}' \frac{1}{2}|\boldsymbol{u}(\boldsymbol{k},t)\,|^2, \tag{3.2}$$

where $\sum_{\boldsymbol{k}}'$ means the summation over the spherical shell within $k-1/2 < |\boldsymbol{k}| \leqslant k+1/2$. The Taylor microscale Reynolds number is defined by

$$R_\lambda(t) \equiv \sqrt{\frac{2E(t)}{3}}\frac{\lambda(t)}{\nu_s}, \tag{3.3}$$

where $E(t)$ and $\lambda(t)$ are the kinetic fluid energy per unit volume

$$E(t) = \frac{1}{V}\int_V \frac{1}{2}\boldsymbol{u}\,(\boldsymbol{x},t)^2\ \mathrm{d}\boldsymbol{x} \equiv \frac{1}{2}\,\langle \boldsymbol{u}^2\rangle_V \tag{3.4}$$

and the Taylor microscale

$$\lambda(t) = \frac{\langle u_1^2 \rangle_V^{1/2}}{\left\langle \left(\dfrac{\partial u_1}{\partial x_1} \right)^2 \right\rangle_V^{1/2}}, \tag{3.5}$$

respectively. The initial value of R_λ is $R_\lambda(0) = 52$. The Kolmogorov length and time scales, $l_K(t)$ and $\tau_K(t)$, are respectively defined by

$$l_K(t) = \left(\frac{\nu_s^3}{\varepsilon(t)} \right)^{1/4}, \tag{3.6}$$

$$\tau_K(t) = \left(\frac{\nu_s}{\varepsilon(t)} \right)^{1/2}, \tag{3.7}$$

where $\varepsilon(t)$ is the mean energy dissipation rate per unit mass

$$\varepsilon(t) = \nu_s \langle (\boldsymbol{\nabla u})^2 \rangle_V . \tag{3.8}$$

Here l_K and τ_K are evaluated using the maximum value ε_{max} of $\varepsilon(t)$ in the one-way coupled case, and they are used to determine several parameters. Here $l_K(t)$ was always larger than the grid spacing Δx, i.e. the velocity field is adequately resolved at small scales.

Initially, the dumbbells are uniformly and randomly distributed over the computational domain. The initial configuration of each dumbbell is set by $\boldsymbol{R}^{(m)}(0) = \sqrt{3} r_{eq} \boldsymbol{n}^{(m)}$, where $\boldsymbol{n}^{(m)}$ is the random unit vector, which is isotropically distributed. Time integration of (2.1) and (2.2) is performed by a similar method to that proposed by Celani *et al.* (2005*b*), where the velocity components at each bead position are interpolated using a TS13 scheme (Yeung & Pope 1988). A multi-time step is used for the temporal evolution of $\boldsymbol{R}^{(n)}(t)$, where the time increment Δt_p for $\boldsymbol{R}^{(n)}(t)$ is chosen by $\Delta t_p = \Delta t_{DNS}/N_{fine}$ when $|\boldsymbol{R}^{(n)}(t)| > 0.9 L_{max}$, while $\Delta t_p = \Delta t_{DNS}$ for $|\boldsymbol{R}^{(n)}(t)| < 0.9 L_{max}$. Here N_{fine} is the number of sub-steps with a finer time increment and is appropriately chosen for the sake of stable numerical integration when W_i is large. This requires a greater computational cost.

Parallel computations are performed to evaluate the convection and deformation of the dispersed dumbbells. The program is parallelized by using the message passing interface (MPI). The maximum number of MPI processors is 256. The total number of dumbbells, $\tilde{N}_t$, is divided into M groups, with each group assigned one processor that computes their temporal evolution. One processor is also assigned to perform the DNS of the solvent fluid, i.e. we use $M + 1$ processors for the total system. The field data of the fluid velocity $\boldsymbol{u}(\boldsymbol{x}, t)$ from the process dedicated to the time integration of the turbulence is transferred to all of the other M processes for the computation of the polymers. The reaction of the polymers is evaluated as follows.

(*a*) The polymer stress field $\boldsymbol{T}_m^p(\boldsymbol{x})$ $(m = 1, \ldots, M)$ is computed according to (2.10) in each processor.

(*b*) These are gathered by the processor $(m = 0)$ for the turbulence DNS and summed as $\boldsymbol{T}^p(\boldsymbol{x}) = \sum_{m=1}^{M} \boldsymbol{T}_m^p(\boldsymbol{x})$.

(*c*) The obtained $\boldsymbol{T}^p(\boldsymbol{x})$ is incorporated into the DNS of the NS equations.

In step (*a*), because the centre-of-mass vector $\boldsymbol{r}_g^{(n)}$ for each of the dumbbells is not on the grid points for the DNS computation, we need an approximate expression

	$\tilde{N}_t$ $(\times 10^9)$	b $(\times 10^5)$	$\Phi_V(\times 10^{-4})$	η	β	W_i	τ
Run A	1.008	0.9	2.02	0.2090	0.827	5	0.981
Run E1	0.504	0.9	1.01	0.1045	0.905	5	0.981
Run E2	1.008	0.9	2.02	0.2090	0.827	5	0.981
Run E3	2.016	0.9	4.04	0.4180	0.705	5	0.981
Run W1	0.504	0.9	1.01	0.1045	0.905	1	0.196
Run W2	0.504	0.9	1.01	0.1045	0.905	25	4.903
Run L	0.126	7.2	2.02	0.2090	0.827	5	0.981
Run H	8.064	0.1125	2.02	0.2090	0.827	5	0.981
Run F	1.008	0.9	2.02	0.2090	0.827	5	0.981

TABLE 1. Parameters for the DNS of decaying turbulence and Brownian dynamics simulation for dispersed dumbbells. Run A refers to the one-way coupled case. Run F has the same physical parameters as Run E2 but is performed using 256^3 grid points.

instead of (2.10). The delta function in (2.10) is approximated by the weight function $\delta_\Delta(\boldsymbol{x} - \boldsymbol{r}_g^{(n)})$ used for the linear interpolation scheme (Prosperetti & Tryggvason 2007). This is expressed by

$$\delta_\Delta(\boldsymbol{x} - \boldsymbol{r}_g^{(n)}) = d_\Delta(x_1 - r_{g,1}^{(n)}) d_\Delta(x_2 - r_{g,2}^{(n)}) d_\Delta(x_3 - r_{g,3}^{(n)}), \tag{3.9}$$

with

$$d_\Delta(x) = \begin{cases} \dfrac{1}{\Delta}\left(1 - \dfrac{|x|}{\Delta}\right) & (|x| \leqslant \Delta) \\ 0 & (|x| > \Delta) \end{cases} \tag{3.10}$$

where Δ was chosen by the grid spacing Δx.

The elastic nature of the dumbbell is controlled by W_i, and the concentration of the polymer solution is determined by η. We performed a series of simulations as follows: (i) η dependence for fixed W_i; (ii) W_i dependence for fixed η; and (iii) $\tilde{N}_t$ dependence for fixed W_i, η and N_t. The third case is performed to evaluate the validity of the replica assumption, which is used in constructing the polymer stress tensor. The parameters used for the simulations are summarized in table 1.

4. Modification of decaying isotropic turbulence

Before presenting our numerical results, we discuss the fundamental nature of decaying isotropic turbulence with polymer additives. A similar discussion is found in a previous paper by Cai *et al.* (2010) for the case of the FENE-P model.

A fundamental quantity of decaying turbulence is the kinetic fluid energy per unit volume $E(t)$, which is defined by (3.4). The temporal evolution of $E(t)$ is derived from (2.9) as

$$\frac{\mathrm{d}E}{\mathrm{d}t} = -\varepsilon(t) - \varepsilon_p(t). \tag{4.1}$$

The term $\varepsilon_p(t)$ represents the polymer effects on the energy decay, which is defined by

$$\varepsilon_p(t) = \langle \partial_i u_j T_{ij}^p \rangle_V = \langle S_{ij} T_{ij}^p \rangle_V, \tag{4.2}$$

where $S_{ij} = (\partial_i u_j + \partial_j u_i)/2$. This term originates from the polymer stress field added to the NS equations and contributes to the energy exchange between the turbulence and

the ensemble of dumbbells. In order to understand the role of $\varepsilon_p(t)$, we consider the variation of the elastic energy $U(t)$ of the ensemble of dumbbells, defined by

$$U(t) = -\frac{\nu_s \eta}{2\tau}\left(\frac{L_{max}}{r_{eq}}\right)^2 \frac{1}{N_t}\sum_{m=1}^{N_t} \ln\left[1 - \left(\frac{|\boldsymbol{R}^{(m)}(t)|}{L_{max}}\right)^2\right]. \tag{4.3}$$

The time evolution is expressed as

$$\frac{\mathrm{d}}{\mathrm{d}t}U(t) = \varepsilon_p'(t) - \varepsilon_S(t) + \varepsilon_B(t), \tag{4.4}$$

where $\varepsilon_S(t)$ and $\varepsilon_B(t)$ are defined as

$$\varepsilon_S(t) = \frac{\nu_s \eta}{2\,(\tau r_{eq})^2}\frac{1}{N_t}\sum_{m=1}^{N_t}\left(\boldsymbol{R}^{(m)} f\left(\frac{|\boldsymbol{R}^{(m)}|}{L_{max}}\right)\right)^2, \tag{4.5}$$

$$\varepsilon_B(t) = \frac{\nu_s \eta}{\sqrt{2\tau^3} r_{eq}}\frac{1}{N_t}\sum_{m=1}^{N_t} R_\alpha^{(m)} \delta w_\alpha^{(m)} f\left(\frac{|\boldsymbol{R}^{(m)}|}{L_{max}}\right). \tag{4.6}$$

The terms ε_S and ε_B are the work done by the elastic force and the work done by the thermal agitation, respectively.

The term $\varepsilon_S(t)$ works to suppress the increase of elastic energy due to the elastic force among the beads because of $\varepsilon_S(t) > 0$. Here $\varepsilon_B(t)$ is expected to be smaller than $\varepsilon_p'(t)$ because we are considering the case of stretching dumbbells. The term $\varepsilon_p'(t)$ is defined by

$$\varepsilon_p'(t) = \frac{\nu_s \eta}{\tau r_{eq}^2}\frac{1}{N_t}\sum_{m=1}^{N_t}(u_\alpha(\boldsymbol{x}_1^{(m)}) - u_\alpha(\boldsymbol{x}_2^{(m)}))R_\alpha^{(m)} f\left(\frac{|\boldsymbol{R}^{(m)}|}{L_{max}}\right). \tag{4.7}$$

Note that $\varepsilon_p'(t) = \varepsilon_p(t)$ (4.2) because of Newton's third law. If $\varepsilon_p'(t) > 0$, the ensemble of dumbbells absorbs kinetic energy from the fluid motion, while for $\varepsilon_p'(t) < 0$, the elastic energy stored in the ensemble of dumbbells is released and transferred to the fluid. If the fluid motion plays only a minor part in the dumbbell dynamics, as is the case for $W_i \ll 1$, we expect $\varepsilon_p'(t) \simeq 0$. In this case, the dumbbells remain in a thermal equilibrium state, yielding the expected values of $U(t) \simeq 3\nu_s\eta/2\tau$ and $\varepsilon_S(t) = \varepsilon_B(t) \simeq 3\nu_s\eta/2\tau^2$.

The above discussion indicates that the effect of polymer additives on the energy decay originates from: (i) removing/adding energy from/to the turbulent flow via $\varepsilon_p(t)$; and (ii) the modification of $\varepsilon(t)$ itself by the polymer additives. The modification in the second case is further examined by considering the equation of motion for the enstrophy $E_\omega(t) = \langle\boldsymbol{\omega}^2\rangle_V/2$ with $\boldsymbol{\omega} = \nabla\times\boldsymbol{u}$ because of $\varepsilon(t) = 2\nu_s E_\omega(t)$ for the isotropic turbulence. From (2.9) we have

$$\frac{\mathrm{d}}{\mathrm{d}t}E_\omega(t) = \langle\boldsymbol{\omega}\cdot(\boldsymbol{\omega}\cdot\nabla\boldsymbol{u})\rangle_V + \langle(\nabla\times\boldsymbol{\omega})\cdot(\nabla:\boldsymbol{T}^p)\rangle_V - \nu_s\langle(\nabla\boldsymbol{\omega})^2\rangle_V, \tag{4.8}$$

where the first term of the right-hand side (RHS) of (4.8) originates from the vorticity-stretching term, which increases or decreases vorticity through the rate of strain tensor. Polymer effects appear directly in the second term and the third term represents the enstrophy dissipation by the viscosity which is always negative. If the statistics of the turbulent field is isotropic, the relationship

$$\langle\boldsymbol{\omega}\cdot(\boldsymbol{\omega}\cdot\nabla\boldsymbol{u})\rangle_V = -\tfrac{7}{3}\sqrt{\tfrac{2}{15}}S(t)E_\omega(t)^{3/2} \tag{4.9}$$

is satisfied for the period of decay, where $S(t)$ is the normalized third-order moment (skewness) of the longitudinal velocity derivative $\partial u_1/\partial x_1$ defined by

$$S(t) = \frac{\left\langle \left(\frac{\partial u_1}{\partial x_1} \right)^3 \right\rangle_V}{\left\langle \left(\frac{\partial u_1}{\partial x_1} \right)^2 \right\rangle_V^{3/2}}. \tag{4.10}$$

The sign of $S(t)$ directly relates to the increase or decrease of the enstrophy, where $S(t) < 0$ and > 0 enhances and inhibits the production of enstrophy, respectively. However, if we consider the high-Reynolds-number case for decaying turbulence without polymer additives, dimensional analysis predicts that the first term of the RHS of (4.8) balances with the third term (Tennekes & Lumley 1972), implying that the mean enstrophy is almost unchanged. When we consider the high-Reynolds-number case with polymer additives, the situation becomes more complicated, and the evolution of $E_\omega(t)$ when the polymers are present should be examined by exploring the contributions of all of the terms in (4.8). We discuss the effects of polymer additives on the behaviour of enstrophy by investigating the contributions of the terms in the RHS of (4.8) to the enstrophy production or inhibition through changes in η and W_i.

The statistical nature of the ensemble of dumbbells is characterized by the probability density function (p.d.f.) of the end-to-end distance $|\boldsymbol{R}^{(n)}(t)|$, which is defined by

$$P(R, t) = \frac{1}{N_t} \sum_{n=1}^{N_t} \delta(R - |\boldsymbol{R}^{(n)}(t)|). \tag{4.11}$$

Theoretical analysis predicts a power-law decay of $P(R) \sim R^{-1+\beta}$ with β dependent on W_i and the spatial dimensions (Balkovsky *et al.* 2000; Chertkov 2000; Thiffeault 2003; Afonso & Vincenzi 2005; Celani *et al.* 2005*a*). The coil–stretch transition occurs at the critical W_i value in isotropic steady turbulence (Watanabe & Gotoh 2010) with the p.d.f. form characterized by $\beta = 0$, i.e. $P(R) \sim R^{-1}$ in the range $r_{eq} \ll R \ll L_{max}$. It is appropriate to investigate the coil–stretch transition for the case of steady turbulence because the dumbbells' statistics for various values of W_i are well-defined irrespective of the time. Here, we discuss only changes in the p.d.f. by varying the parameters η and W_i during a period of decay.

It is interesting to see how polymer additives modify the behaviour of $E(k, t)$. Since the Reynolds number for the turbulent system discussed here ($R_\lambda < 50$) is as low as $R_\lambda < 50$, there is no inertial range. The evolution equation for $E(k, t)$ is

$$\frac{\partial}{\partial t} E(k, t) = -2\nu_s k^2 E(k, t) + T(k, t) + T_p(k, t), \tag{4.12}$$

where $T(k, t)$ is the energy transfer function, and the term $T_p(k, t)$ is due to the polymers. From the definition, we must have $\int_0^\infty T(k, t)\,\mathrm{d}k = 0$ and $\int_0^\infty T_p(k, t)\,\mathrm{d}k = -\varepsilon_p(t)$. We investigate how $T(k, t)$ and $T_p(k, t)$ contribute to the energy budget in the wavenumber space and how they depend on the parameters η and W_i.

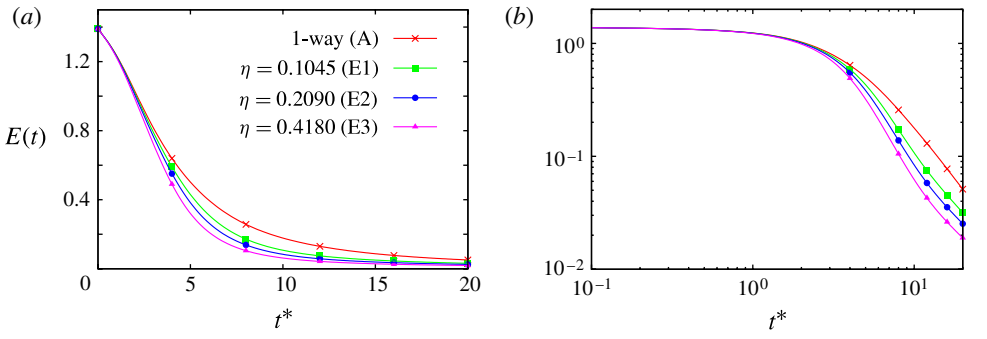

FIGURE 1. (Colour online) Effect of η on the temporal evolution of the kinetic energy $E(t)$ for: (*a*) a linear plot; and (*b*) a log–log plot.

We define several scales to characterize the turbulent motion. The largest scale of turbulent motion is represented by the integral scale $L(t)$, which is defined by

$$L(t) = \frac{3\pi}{4E(t)} \int_0^\infty k^{-1} E(k, t)\, \mathrm{d}k. \tag{4.13}$$

The Kolmogorov length scale $l_K(t)$ (3.6) defines the smallest scale in the turbulence. The Taylor microscale $\lambda(t)$ (3.5) is also a characteristic scale of the turbulence. In general, we have $L(t) > \lambda(t) > l_K(t)$ for the DNS of isotropic turbulence. Because we are considering polymer-laden flow, the relaxation time of a dumbbell, τ, introduces an additional characteristic length. This is referred to as the Lumley scale $l_L(t)$ (Lumley 1973) and is defined by

$$l_L(t) = \left(\tau^3 \varepsilon(t)\right)^{1/2}. \tag{4.14}$$

The Lumley scale represents the scale at which the characteristic time in the inertial range ($\sim \varepsilon^{-1/3} r^{2/3}$) equals τ. Note that l_L is also represented in terms of l_K as $l_L(t) = (\nu_s \tau)^{3/2} / (l_K(t))^2 = (W_i^*(t))^{3/2}\, l_K(t)$ by using (3.6) and (4.14), where we define the instantaneous Weissenberg number by $W_i^*(t) \equiv \tau / \tau_K(t)$. Typical values of the above-mentioned length scales are summarized in table 2.

5. Results

5.1. *Concentration effects*

In this section, we examine how a turbulent flow with polymer additives is modified by changing the parameter η for fixed W_i (=5). Hereafter, we use the non-dimensional time t^* defined as $t^* = t u_0 k_0$.

Figure 1 shows the temporal evolution of the kinetic fluid energy $E(t)$ for a one-way simulation (Run A), $\eta = 0.1045$ (Run E1), $\eta = 0.2090$ (Run E2) and $\eta = 0.4180$ (Run E3). It is found that the kinetic energy monotonically decays with time, and the rate of decay increases with η. We also observe a near power-law decay behaviour ($E(t) \sim t^{-\gamma}$) in the later time of figure 1(*b*), with the exponent γ increasing with η. Figure 2 presents the temporal evolutions of: (*a*) the energy dissipation rate $\varepsilon(t)$; and (*b*) the energy transfer $\varepsilon_p(t)$ caused by the polymer additives. The peak positions for each $\varepsilon(t)$ curve are at around $t^* \simeq 2$ and $\varepsilon(t)$ decays with time for $t^* > 2$ irrespective of η. The decay of $\varepsilon(t)$ becomes faster for larger η. For various values of η, the peak positions of $\varepsilon_p(t)$ are located at later times ($t^* = 3 \sim 5$) than those of $\varepsilon(t)$.

https://doi.org/10.1017/jfm.2012.595 Published online by Cambridge University Press

t^*	2	4	8	16
Run A	(0.0577, 0.627, 1.093)	(0.0630, 0.591, 1.058)	(0.0830, 0.650, 1.208)	(0.129, 0.858, 1.496)
Run E1	(0.0580, 0.631, 1.096)	(0.0660, 0.614, 1.088)	(0.0991, 0.757, 1.356)	(0.163, 1.045, 1.702)
Run E2	(0.0583, 0.634, 1.099)	(0.0673, 0.626, 1.109)	(0.1073, 0.797, 1.421)	(0.179, 1.126, 1.800)
Run E3	(0.0588, 0.639, 1.105)	(0.0705, 0.646, 1.148)	(0.1178, 0.835, 1.490)	(0.202, 1.229, 1.893)
Run W1	(0.0583, 0.635, 1.100)	(0.0647, 0.608, 1.077)	(0.0862, 0.680, 1.239)	(0.134, 0.896, 1.531)
Run W2	(0.0578, 0.629, 1.094)	(0.0647, 0.602, 1.080)	(0.1054, 0.708, 1.460)	(0.192, 0.780, 1.715)

TABLE 2. Summary of the values of the characteristic length scales (l_K, λ, L) at $t^* = 2, 4, 8$ and 16 for Runs A, E1, E2, E3, W1 and W2. The Lumley scale l_L (4.14) is evaluated by the relationship $l_L = (\nu_s \tau)^{3/2} l_K^{-2}$.

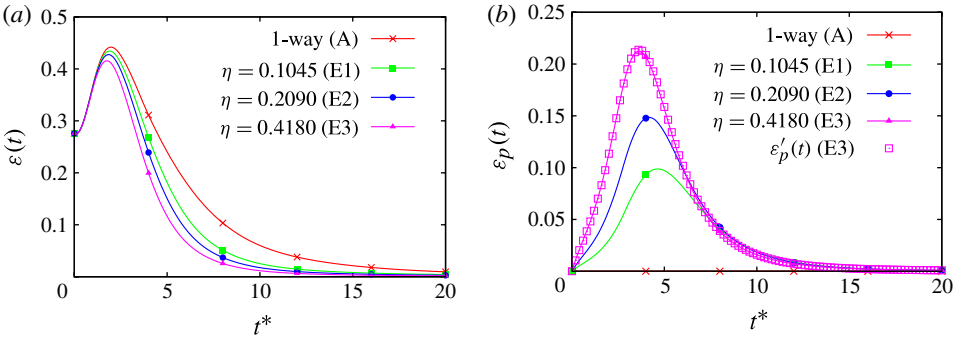

FIGURE 2. (Colour online) Effect of η on the temporal evolution of: (*a*) the energy dissipation rate $\varepsilon(t)$; and (*b*) the energy transfer $\varepsilon_p(t)$ by polymer additives. Note that $\varepsilon_p(t) = \varepsilon'_p(t)$ for Run E3.

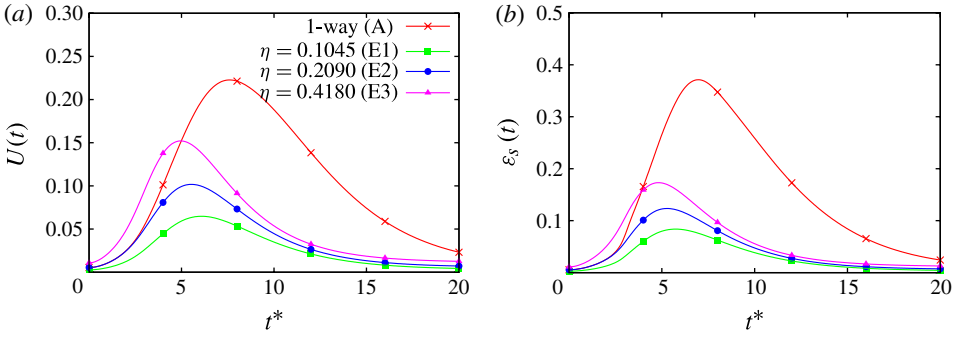

FIGURE 3. (Colour online) Effect of η on the temporal evolution of (*a*) the elastic energy $U(t)$ and (*b*) the rate of loss of the elastic energy $\varepsilon_S(t)$.

Moreover, $\varepsilon_p(t)$ increases with η, suggesting enhanced energy extraction from the turbulent motion for larger concentrations, as shown in figure 1. Note that the equality $\varepsilon_p(t) = \varepsilon'_p(t)$ holds in Run E3. The observed responses of $E(t)$ and $\varepsilon(t)$ suggest that the extended dumbbells significantly affect the turbulent motion over all scales, qualitatively consistent with the DNS results previously obtained by using the FENE-P model (Perlekar *et al.* 2006; Cai *et al.* 2010).

Figure 3 compares the curves for: (*a*) the elastic energy $U(t)$; and (*b*) the loss of elastic energy $\varepsilon_S(t)$. For two-way cases when $E(t)$ decreases with time, the corresponding $U(t)$ increases from its initial value for times up to $t^* \simeq 5$. This demonstrates the energy transfer from the turbulent motion to the ensemble of dumbbells due to $\varepsilon_p(t)$. The elastic energy increases with η for two-way cases, although that of the one-way case is the largest among these calculations. The passively advected dumbbells (Run A) are more stretched than the two-way cases, resulting in more elastic energy being stored. This is due to the lack of back reaction on the fluid motion, which plays a role in decreasing the turbulence kinetic energy, leading to suppression of dumbbell extension. This observation is also consistent with the results of DNSs using the constitutive equations (Eckhardt *et al.* 2002; Perlekar *et al.* 2006). It is interesting to note that the peak positions of both $\varepsilon_S(t)$ and $U(t)$

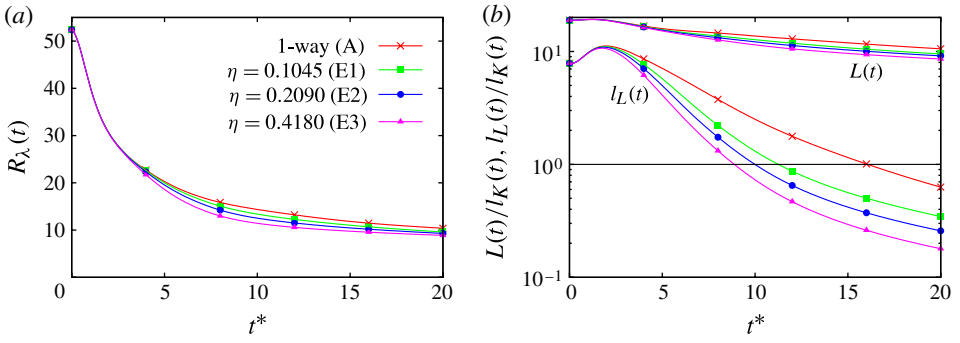

FIGURE 4. (Colour online) Effect of η on the temporal evolution of: (*a*) the Taylor micro-scale Reynolds number $R_\lambda(t)$; and (*b*) the integral and Lumley length scales divided by the Kolmogorov length scale, $L(t)/l_K(t)$ and $l_L(t)/l_K(t)$, respectively.

remain almost unchanged when η is varied. The time t_p defined as $dU(t_p)/dt = 0$ gives $\varepsilon_S(t_p) \simeq \varepsilon_p'(t_p)$. At around t_p, the gain of elastic energy through the fluid motion is balanced with the losses due to the elastic force.

Figure 4 shows the temporal evolutions of: (*a*) the Taylor micro-scale Reynolds number $R_\lambda(t)$; and (*b*) the integral and Lumley length scales divided by the Kolmogorov length scale, $L(t)/l_K(t)$ and $l_L(t)/l_K(t)$, respectively. Here $R_\lambda(t)$ monotonically decays with time, and its behaviour is almost insensitive to changes in η. At the end of the simulated time ($t^* = 20$), $R_\lambda \simeq 10$, irrespective of η. Similar behaviour for the scale ratio $L(t)/l_K(t)$ is also observed in figure 4(*b*). Conversely, the ratio $l_L(t)/l_K(t)$ decreases with increasing η, and all two-way cases are below unity for $t^* > 12$. The behaviour of $l_L(t)/l_K(t)$ implies that the mean elongation of the dumbbells is reduced when η is increased, and that the dumbbell dynamics does not largely affect the turbulent motion for $t^* > 12$.

Figure 5 presents the temporal evolutions for: (*a*) $\langle \boldsymbol{\omega} \cdot (\boldsymbol{\omega} \cdot \nabla \boldsymbol{u}) \rangle_V$; (*b*) $\langle (\nabla \times \boldsymbol{\omega}) \cdot (\nabla : \boldsymbol{T}^p) \rangle_V$; (*c*) $-\nu_s \langle (\nabla \boldsymbol{\omega})^2 \rangle_V$; and (*d*) the sum of all terms in (*a–c*) for several values of η, as well as a one-way case. From figure 5(*a*), it is confirmed that $\langle \boldsymbol{\omega} \cdot (\boldsymbol{\omega} \cdot \nabla \boldsymbol{u}) \rangle_V$ is positive over the entire time region irrespective of η, indicating the contribution to the production of enstrophy. The term $\langle \boldsymbol{\omega} \cdot (\boldsymbol{\omega} \cdot \nabla \boldsymbol{u}) \rangle_V$ attains its maximum value at around $t^* = 1$, irrespective of η, and gradually decreases with time for $t^* > 1$. The decay becomes faster for larger η, meaning that the enstrophy production is suppressed by polymer additives. We will return to this point in a later section. Figure 5(*a*) also suggests a negative skewness factor $S(t)$ during the time evolution, which decreases with increasing η (figure not shown). Interestingly in figure 5(*b*), $\langle (\nabla \times \boldsymbol{\omega}) \cdot (\nabla : \boldsymbol{T}^p) \rangle_V$ is positive for $t^* > 3$, with a maximum value at around $t^* = 5$ which is larger than $\langle \boldsymbol{\omega} \cdot (\boldsymbol{\omega} \cdot \nabla \boldsymbol{u}) \rangle_V$ in Runs E2 and E3 at the same time. This indicates that on average, the polymer stress produces the enstrophy after $t^* = 3$, and the production of it increases with η. The term $-\nu_s \langle (\nabla \boldsymbol{\omega})^2 \rangle_V$ shows a similar η-dependence to that of the vorticity stretching term when $t^* < 3$, as shown in figure 5(*c*). For $t^* > 3$ the amplitude of the enstrophy dissipation decreases with time, and the decay is slower than that of the vorticity stretching amplitude irrespective of η. Also, the temporal evolutions of the sum of all terms in the RHS of (4.8) show that the increase/decrease rate of enstrophy is insensitive to the variation of η. They are negative for $t^* > 2$, where the curve for the one-way case deviates from the others. These observations indicate that the effect of polymer additives on the decay of $\varepsilon(t)$

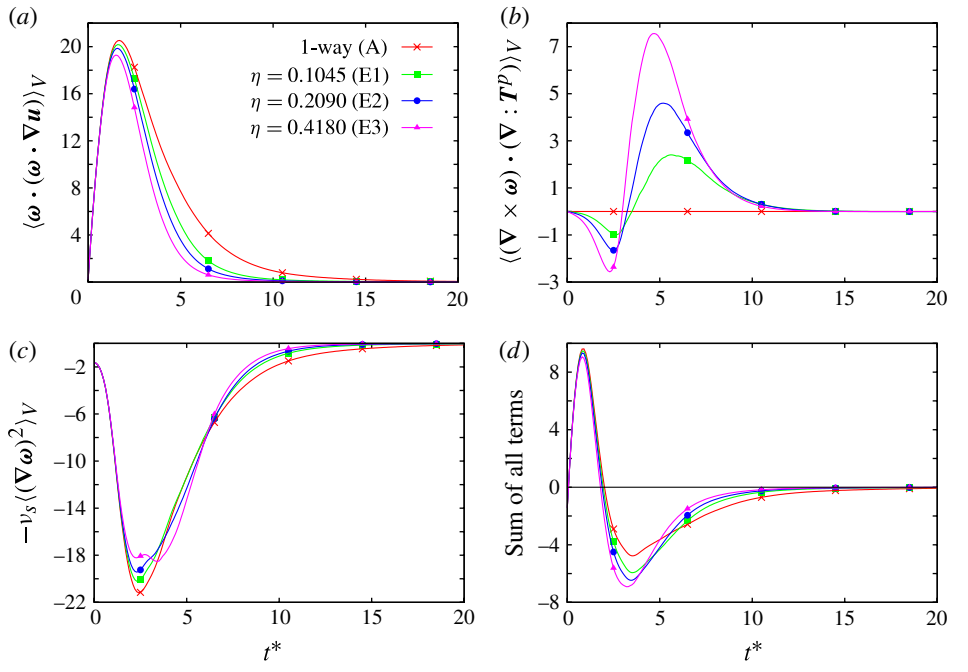

FIGURE 5. (Colour online) Comparison of the temporal evolutions of the terms in the RHS of (4.8): (*a*) $\langle \boldsymbol{\omega} \cdot (\boldsymbol{\omega} \cdot \boldsymbol{\nabla u}) \rangle_V$; (*b*) $\langle (\boldsymbol{\nabla} \times \boldsymbol{\omega}) \cdot (\boldsymbol{\nabla} : \boldsymbol{T}^p) \rangle_V$; (*c*) $-\nu_s \langle (\boldsymbol{\nabla \omega})^2 \rangle_V$; and (*d*) the sum of all terms in (*a–c*) for several values of η.

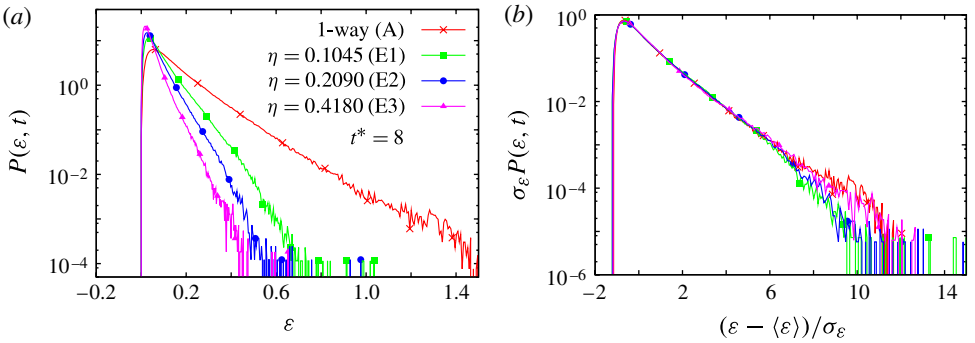

FIGURE 6. (Colour online) Comparison of the p.d.f. behaviour of the fluctuations of the local energy dissipation rate $\tilde{\varepsilon}(\boldsymbol{x}, t)$ for various η using (*a*) bare variables and (*b*) normalized variables.

for $t^* > 2$ is mostly due to the increase of the amplitude of the polymer stress and the decrease of the amplitude of the vorticity stretching. However, the contribution of the enstrophy dissipation term to the decay of $E_{\boldsymbol{\omega}}(t)$ is strongest among the three, leading to a greater dissipation reduction for larger η.

A reduction in the energy dissipation rate is also clearly shown in the behaviour of the p.d.f. of the local energy dissipation $\tilde{\varepsilon}(\boldsymbol{x}, t) = 2\nu_s S_{ij} S_{ij}$, shown in figure 6 at $t^* = 8$. In figure 6(*a*), the probability of finding an intense value of $\tilde{\varepsilon}(\boldsymbol{x}, t)$ decreases

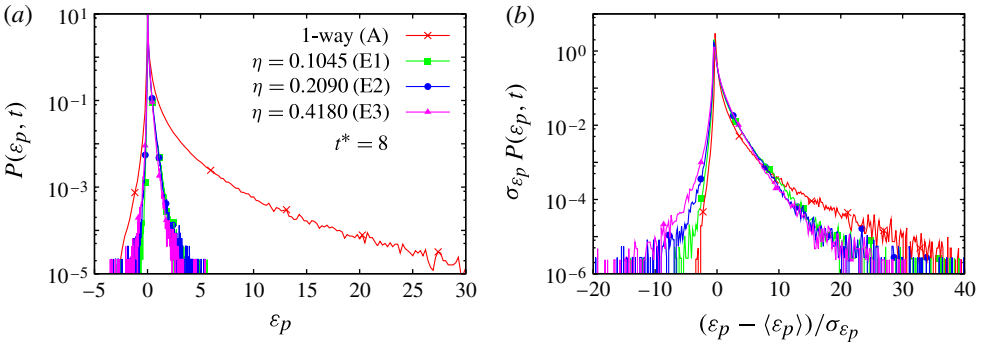

FIGURE 7. (Colour online) Comparison of the p.d.f. behaviour for fluctuations of the local production/inhibition rate $\tilde{\varepsilon}_p(\boldsymbol{x}, t)$ of the turbulence kinetic energy due to the polymer stress for various η cases using (a) bare variables and (b) normalized variables.

with increasing η. Thus, the polymer additives reduce not only the mean value of the energy dissipation, but also the entire intensity of the fluctuations. An interesting observation in the behaviour of the normalized p.d.f. is shown in figure 6(b). The p.d.f. curves almost collapse onto a single curve, irrespective of η, for $(\varepsilon - \bar{\varepsilon})/\sigma_\varepsilon < 6$. Similar results could be observed for the data at different times. We therefore assert that although the behaviour of the p.d.f. itself is affected by polymer additives, its functional form when it is normalized is robust for the variations of η considered here. These results are consistent with those obtained by DNSs of the FENE-P model (Perlekar *et al.* 2010), and are similar to experimental observations examining the p.d.f. of vorticity fluctuations (Liberzon *et al.* 2005, 2006) and fluid particle accelerations (Crawford *et al.* 2008).

The p.d.f. behaviour of the local value of $\varepsilon_p(t)$, $\tilde{\varepsilon}_p(\boldsymbol{x}, t) = S_{ij} T^p_{ij}$, is shown in figure 7. The resulting curves are positively skewed, indicating that on average, the polymers remove the kinetic fluid energy from the turbulent motions. This is consistent with the observation that the polymer additives enhance the kinetic energy decay, as previously shown in figure 1. We also observe that the one-way case is skewed more than the two-way cases because of the lack of the back reaction to fluid motion. The normalized p.d.f. in figure 7(b) also indicates that the p.d.f. form for the positive region is insensitive to variations in η. The p.d.f. form in the negative region, where $\tilde{\varepsilon}_p$ contributes to the energy transfer from the ensemble of dumbbells to the fluid motion, depends on η, and the p.d.f. tail becomes longer as η increases.

Next, we investigate the temporal evolutions of the p.d.f. for the end-to-end distance $|\boldsymbol{R}^{(n)}|/L_{max}$ of the dumbbell. These are shown in figure 8 for Runs A, E1, E2 and E3 with (a) $t^* = 2$, (b) $t^* = 4$ and (c) $t^* = 8$. Figure 8(d) presents the temporal variation of the mean dumbbell extension $\langle|\boldsymbol{R}^{(n)}|\rangle$ normalized by $L_{eq} \equiv \sqrt{3} r_{eq}$. Figure 8($a$) shows only slight changes in the curves as η is varied, and the peak positions of the p.d.f. are located near zero, indicating negligible reaction to turbulent flow when $t^* \leqslant 2$. As time progressed beyond $t^* = 2$, the dumbbells are stretched. At $t^* = 4$, a few dumbbells reach values close to L_{max}, and more stretched dumbbells appear for lower values of η. After $t^* \simeq 6$, the dumbbells begin to shrink toward their equilibrium length, as shown in figure 8(c,d). In this process, the shorter tail of the p.d.f. for larger η can be explained by the fact that the strong velocity gradient fluctuations become increasingly suppressed as η increases, as shown in figures 2 and 6. Because the reaction of the

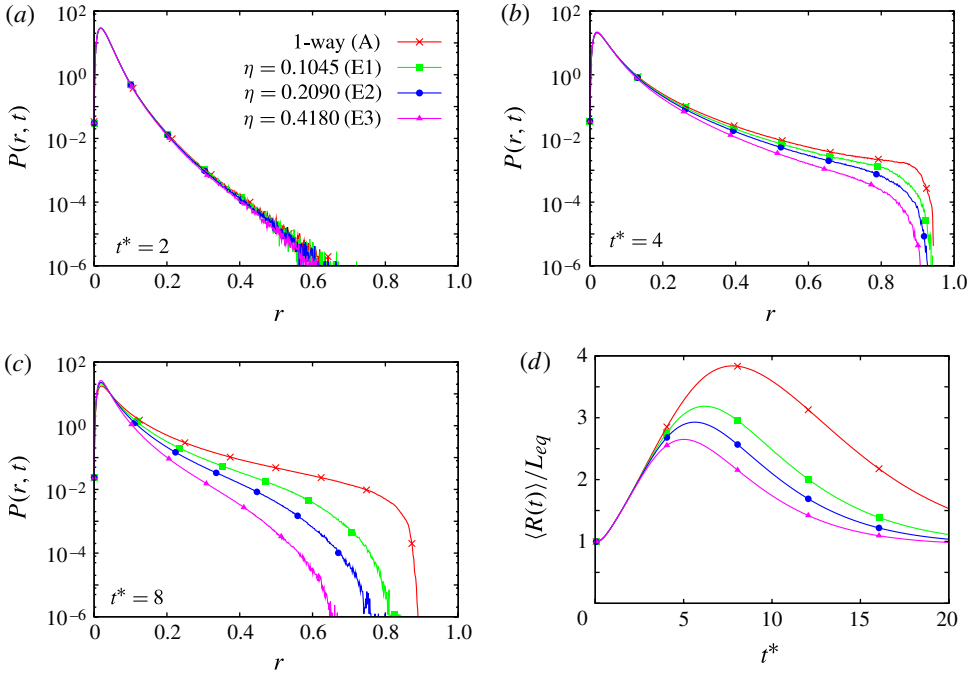

FIGURE 8. (Colour online) Effect of η on the temporal evolution of the polymer extension p.d.f., $P(r, t)$, normalized by the maximum extension length L_{max} for (*a*) $t^* = 2$, (*b*) $t^* = 4$ and (*c*) $t^* = 8$ and (*d*) the temporal evolution of the mean dumbbell extension $\langle|\boldsymbol{R}^{(n)}|\rangle$ divided by $L_{eq} = \sqrt{3}r_{eq}$.

ensemble of dumbbells to the turbulent motion leads to a decrease of the turbulence intensity, the suppression of the dumbbell extensions as η increases is reasonable.

It is interesting to note that the mean end-to-end distance of the ensemble of dumbbells continues to grow even after the energy dissipation rate peaks, where $|\boldsymbol{R}^{(n)}|$ attains a maximum in the decay regime of $\varepsilon(t)$ (figure 2*a*). This fact represents the importance of the persistence of velocity gradient fluctuations experienced by the dumbbells for their stretching efficiency, which is inferred from the Lagrangian correlation time of $\nabla \boldsymbol{u}$ ($\sim 4\tau_K$ by Watanabe & Gotoh (2010)). This was also confirmed in our previous study (e.g., figure 16 in Watanabe & Gotoh (2010)).

To observe the turbulence modifications in more detail, we investigate the behaviour of the kinetic energy spectrum $E(k, t)$ normalized as

$$E(k, t) = \varepsilon\,(t)^{2/3}\, l_K\,(t)^{5/3}\, F(kl_K(t), tu_0k_0, \eta), \tag{5.1}$$

where F is a non-dimensional function depending on k, t and η. Figure 9 compares the spectra for Runs A, E1, E2 and E3 at several times (*a*) $t^* = 2$, (*b*) $t^* = 4$, (*c*) $t^* = 8$ and (*d*) $t^* = 16$. Figure 9(*a*) shows that the spectra are not modified by the polymer additives except for the far tails. After $t^* = 2$, at which $\varepsilon(t)$ begins to decay, the deviation of the curves for the two-way cases from that of the one-way case (Run A) grows in the spectral tail. Interestingly, the normalized spectra given by (5.1) almost collapse onto a single curve for wavenumbers $kl_K(t) < 1$, irrespective of η. That is, $F(kl_K(t), tu_0k_0, \eta) = \tilde{F}(kl_K(t), tu_0k_0)$ for $kl_K(t) < 1$. For the final period of decay ($t^* > 8$), spectral modification is observed over the entire wavenumber range

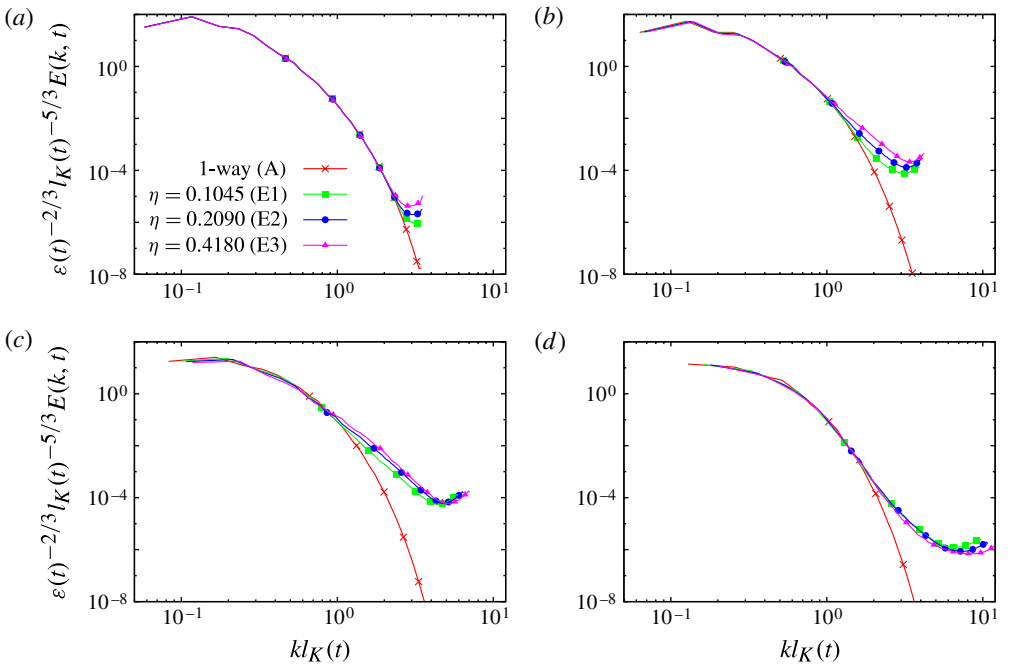

FIGURE 9. (Colour online) Comparison of the kinetic energy spectrum $E(k, t)$ normalized using the Kolmogorov scaling for Runs A, E1, E2 and E3 with (*a*) $t^* = 2$, (*b*) $t^* = 4$, (*c*) $t^* = 8$ and (*d*) $t^* = 16$.

when plotting $E(k, t)$ itself (figure not shown), as demonstrated earlier by the DNS of the FENE-P equation (Vaithianathan & Collins 2003; Perlekar *et al.* 2006; Cai *et al.* 2010). These results suggest that the spectral form normalized by the Kolmogorov unit is not affected by the polymer additives as far as the low wavenumber range is concerned. This mirrors the robustness of the p.d.f. form for $\tilde{\varepsilon}$, shown previously in figure 6(*b*). Figure 9 also matches experimental observations for grid-generated turbulence (McComb *et al.* 1977), where the dimensionless energy spectra of turbulent polymer solution flow with low concentration were almost unchanged. On the other hand, McComb *et al.* (1977) observed that the dissipation range spectra for higher concentrations (more than 250 ppm) showed noticeable attenuations. This raises the question of how the curves in figure 9 would be further modified by even higher concentrations than those considered here.

Figure 10 shows the non-dimensional energy transfer function $\hat{T}(k, t) \equiv T(k, t)/\varepsilon(t) l_K(t)$ at (*a*) $t^* = 4$ and (*b*) $t^* = 8$ for various values of η. For $t^* = 4$, all of the curves collapse onto a single curve, suggesting that at the beginning of the decay, the polymer effects are negligible for the energy transfer. However at the later time ($t^* = 8$) they appear to suppress the extraction of kinetic energy in the small wavenumber range, with an increase of η.

The behaviour of the non-dimensional transfer function $\hat{T}_p(k, t) \equiv T_p(k, t)/\varepsilon(t) l_K(t)$ originating from the polymer additives is also compared in figure 11 at (*a*) $t^* = 4$ and (*b*) $t^* = 8$. In both cases, $\hat{T}_p(k, t)$ is negative for wavenumbers $kl_K(t) < 1$ and almost zero for $kl_K(t) > 1$. This implies that the polymer additives behave as kinetic energy reducers in the spectral equation for wavenumbers $kl_K(t) < 1$. Moreover, their

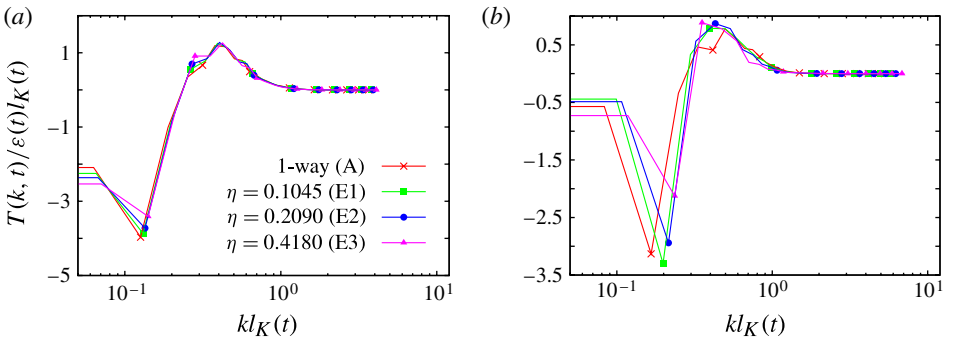

FIGURE 10. (Colour online) Energy transfer function $T(k, t)$ normalized by $\varepsilon(t)l_K(t)$ versus $kl_K(t)$ for various η: (*a*) $t^* = 4$; and (*b*) $t^* = 8$.

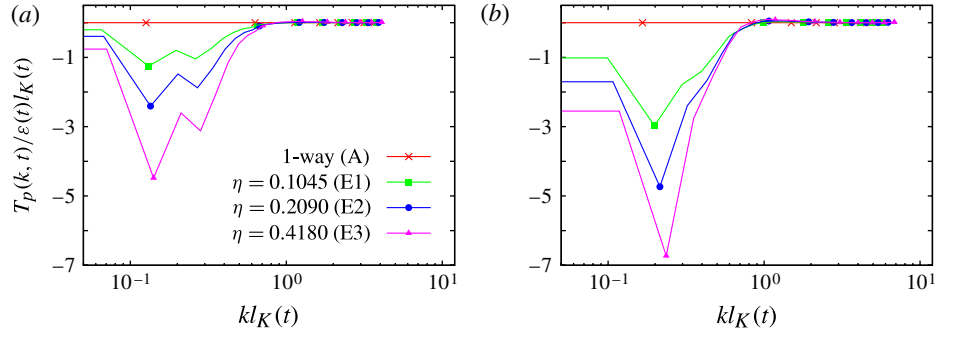

FIGURE 11. (Colour online) Polymer contribution to the energy transfer $T_p(k, t)$ normalized by $\varepsilon(t)l_K(t)$ versus $kl_K(t)$ for various η: (*a*) $t^* = 4$; and (*b*) $t^* = 8$.

amplitudes increase with η, leading to a larger energy reduction rate. This observation is also consistent with the effect of η on the temporal evolution of the kinetic energy $E(t)$ shown in figure 1.

The results of figures 10 and 11 show that although the length of each dumbbell is comparable to or smaller than l_K, their ensemble generates strong effects on the dynamics of turbulence on a scale much larger than l_K. We will return to this point in § 5.3.

5.2. *Weissenberg number effects*

In this subsection, we examine the degree of turbulence modification caused by changes in the Weissenberg number W_i under fixed $\eta(=0.1045)$. Because a large W_i can lead to highly stretched dumbbells, the resulting turbulence modification may be similar to the η-dependence presented in the previous subsection.

Figure 12 shows the temporal evolutions of $E(t)$ for $W_i = 1$, 5, and 25 (Runs W1, E1 and W2, respectively). The $E(t)$ curves collapse onto a single curve for $t^* < 4$. For $t^* > 4$, the decay rate increases with W_i. As shown in figure 12(*b*), the exponent of the near power-law decay of $E(t)$ in this range is clearly dependent on W_i.

The temporal evolutions of the energy dissipation rate $\varepsilon(t)$ and the energy transfer rate $\varepsilon_p(t)$ due to the polymer additives are shown in figure 13 for various values

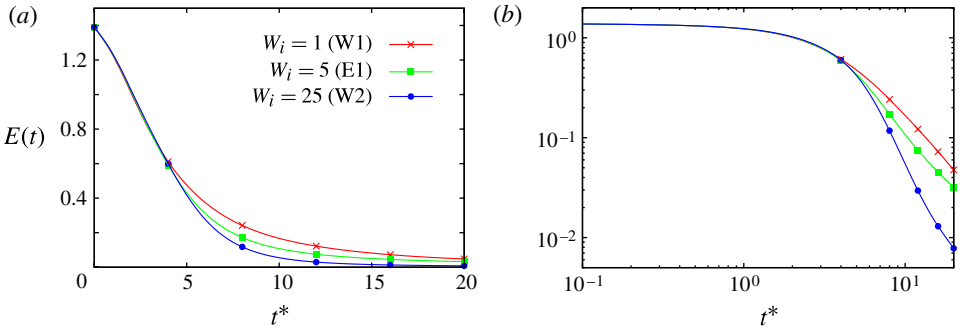

FIGURE 12. (Colour online) Effect of W_i on the temporal evolution of the kinetic energy $E(t)$ for (a) a linear plot and (b) a log–log plot.

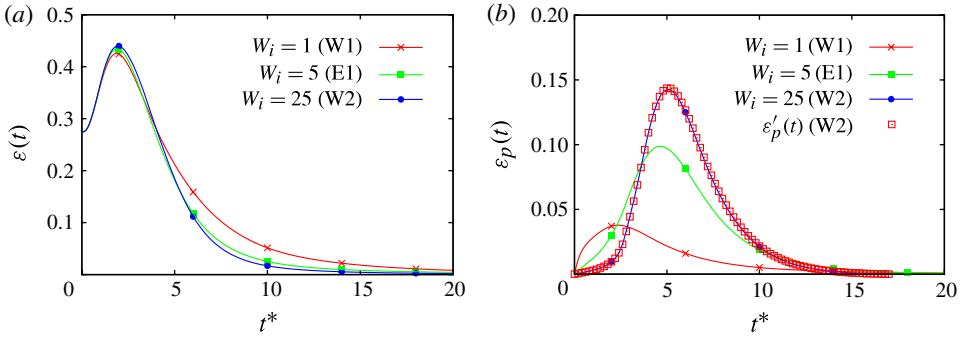

FIGURE 13. (Colour online) Effect of W_i on the temporal evolution of (a) the energy dissipation rate $\varepsilon(t)$ and (b) the energy transfer by polymer additives $\varepsilon_p(t)$.

of W_i. The peak values of $\varepsilon(t)$ for larger W_i are close to that of the one-way case (cf. figure 2a). This is caused by the small number of stretched dumbbells until $t^* \simeq 2$, as will be shown later in figure 19(a). Because the factor $1/\tau$ is contained in T^p_{ij}, the back reaction to the fluid motion is reduced when W_i is larger and $|\boldsymbol{R}^{(n)}|$ is much smaller. A stronger reduction of the energy dissipation for larger W_i can be clearly seen for $t^* > 4$, where the amplitude of $\varepsilon_p(t)$ increases with W_i, indicating that the energy transfer from the turbulence to the ensemble of dumbbells is enhanced with an increase of W_i. We also confirm $\varepsilon'_p(t) = \varepsilon_p(t)$ for Run W2, as shown in figure 2(b).

Figure 14 compares the curves for the elastic energy $U(t)$ and the loss of elastic energy $\varepsilon_S(t)$ for several values of W_i. The increases in $U(t)$ are dependent on the value of W_i. The time at which $U(t)$ reaches its peak value increases with W_i. This means that the delay of energy transfer from the turbulence to the ensemble of dumbbells becomes significant when W_i is increased. Because a larger W_i means a smaller $1/\tau$, it is plausible that the polymer stress term with $|\boldsymbol{R}^{(n)}| \sim L_{eq}$ contributes less to the energy exchange. When the many dumbbells are fully stretched, the polymer stress contributes significantly to the energy exchanges even when $1/\tau$ is much smaller, leading to the increase of $U(t)$. The elastic energy for $W_i = 1$ is almost unchanged beyond the decay of $E(t)$; thus, the dumbbell motion is not greatly affected by the fluid motion, and the energy transfer from the turbulence to the ensemble of dumbbells

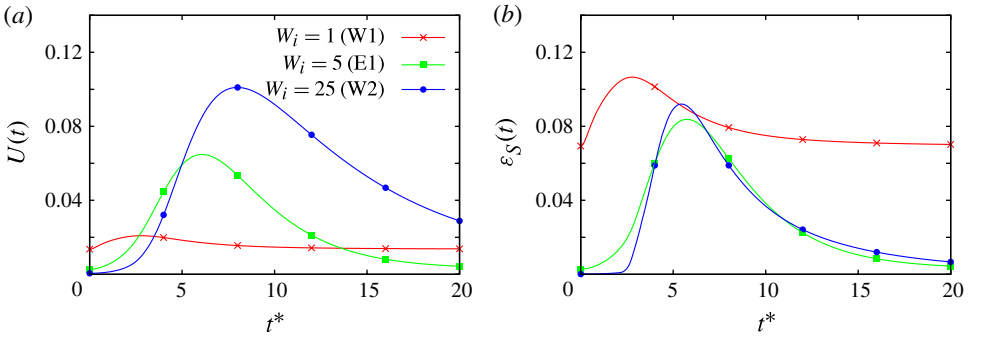

FIGURE 14. (Colour online) Effect of W_i on the temporal evolution of (a) the elastic energy $U(t)$ and (b) the rate of loss of the elastic energy $\varepsilon_S(t)$.

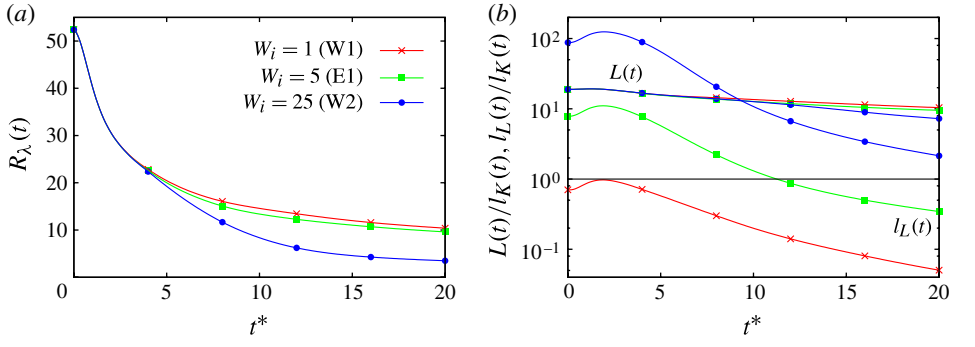

FIGURE 15. (Colour online) Effect of W_i on the temporal evolution of (a) the Taylor micro-scale Reynolds number $R_\lambda(t)$ and (b) the integral and Lumley scales ($L(t)$ and $l_L(t)$) normalized by the Kolmogorov length scale $l_K(t)$.

is not significant for $W_i \leqslant 1$. This also suggests that $U(t)$ is close to its equilibrium value of $U = 3\nu_s\eta/2\tau = 1.36 \times 10^{-2}$, consistent with the value of the curve in the flat region in figure 14(a). For $W_i = 25$, there is active energy transfer by $\varepsilon_p(t)$, leading to a significant increase in $U(t)$. The behaviour of $\varepsilon_S(t)$ shows that the loss of elastic energy for $W_i = 1$ is larger than that for other values of W_i. Because the dumbbells are not sufficiently stretched when $W_i = 1$ and $\varepsilon_S(t)$ is proportional to τ^{-2}, it is plausible that $\varepsilon_S(t)$ becomes larger for smaller W_i. The nearly constant values of $\varepsilon_S(t)$ for $t^* = 20$ can be estimated by its equilibrium value of $\varepsilon_S = 3\nu_s\eta/2\tau^2 = 6.93 \times 10^{-2}$, which is consistent with our results in figure 14(b).

Figure 15 shows the temporal evolutions of (a) the Taylor microscale Reynolds number $R_\lambda(t)$ and (b) the integral and Lumley length scales $L(t)$ and $l_L(t)$ normalized by $l_K(t)$ for various W_i. Here $R_\lambda(t)$ monotonically decays with time and behaves the same for both $W_i = 1$ and 5. The curve of $W_i = 25$ deviates from the others for $t^* > 5$, with significantly different values at the end point of the simulation ($t^* = 20$), where $R_\lambda \simeq 10$ for $W_i = 1$ and 5 and $R_\lambda \simeq 4$ for $W_i = 25$. Thus, there is a clear difference between the nature of the turbulence decay for $W_i = 25$ and the other cases. In figure 15(b), the scale ratio $L(t)/l_K(t)$ decreases with time, and the decay of $W_i = 25$ is slightly faster than for the other cases. Conversely, the scale ratio $l_L(t)/l_K(t)$

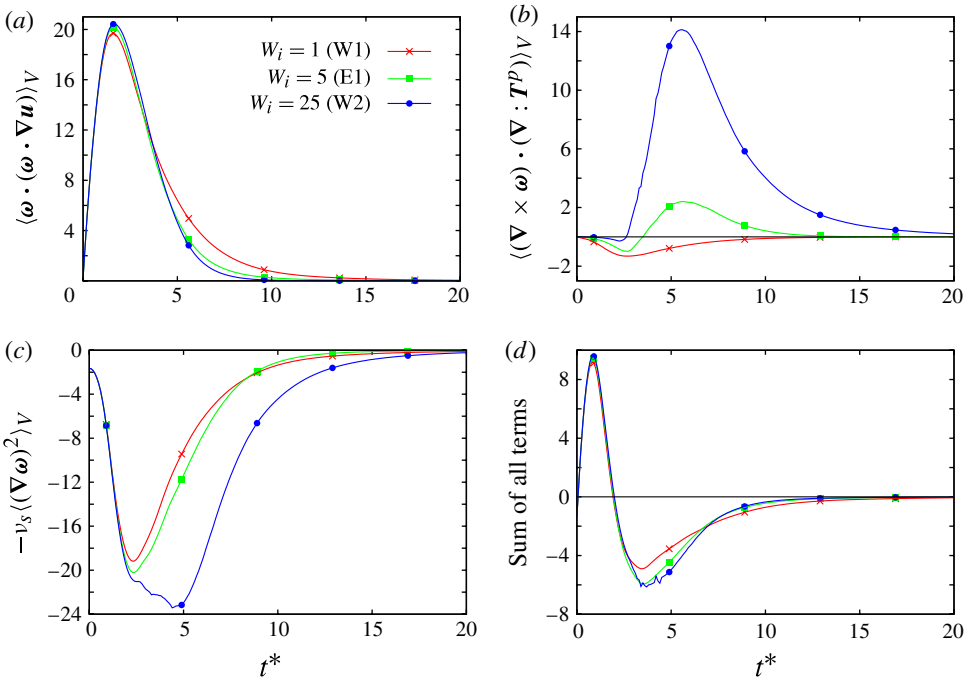

FIGURE 16. (Colour online) Comparison of the temporal evolutions for the terms in the RHS of (4.8): (*a*) $\langle \boldsymbol{\omega} \cdot (\boldsymbol{\omega} \cdot \nabla \boldsymbol{u}) \rangle_V$; (*b*) $\langle (\nabla \times \boldsymbol{\omega}) \cdot (\nabla : \boldsymbol{T}^p) \rangle_V$; (*c*) $-\nu_s \langle (\nabla \boldsymbol{\omega})^2 \rangle_V$; and (*d*) the sum of all terms in (*a–c*) for several values of W_i.

shown in figure 15(*b*) varies with W_i. This is caused by the difference of the values of τ for different W_i. For $W_i = 1$, the ratio $l_L(t)/l_K(t)$ is smaller than unity for all values of time, suggesting there are no significant dumbbell extensions. While for $W_i = 25$, $l_L(t)/l_K(t)$ remains larger than unity, even after the turbulence has decayed. This implies that the influence of the ensemble of dumbbells on the turbulent motion at the scales of l_L is quite large when W_i is large.

Figure 16 compares the curves of; (*a*) $\langle \boldsymbol{\omega} \cdot (\boldsymbol{\omega} \cdot \nabla \boldsymbol{u}) \rangle_V$; (*b*) $\langle (\nabla \times \boldsymbol{\omega}) \cdot (\nabla : \boldsymbol{T}^p) \rangle_V$; (*c*) $-\nu_s \langle (\nabla \boldsymbol{\omega})^2 \rangle_V$; and (*d*) the sum of the all terms in (*a–c*) for various values of W_i. The behaviour of the curves are similar to those obtained for the case when η is varied (figure 5). In figure 16(*a*), the enstrophy production due to the vorticity stretching term attains its maximum value at around $t^* = 2$, and decays with time for $t^* > 2$, where the enstrophy production decreases as W_i is increased. Note that the temporal variation of $\langle \boldsymbol{\omega} \cdot (\boldsymbol{\omega} \cdot \nabla \boldsymbol{u}) \rangle_V$ is very similar to those of $\varepsilon(t)$ (figure 13*a*). A noticeable W_i-dependence is observed in the temporal variations of $\langle (\nabla \times \boldsymbol{\omega}) \cdot (\nabla : \boldsymbol{T}^p) \rangle_V$ in figure 16(*b*). Here $\langle (\nabla \times \boldsymbol{\omega}) \cdot (\nabla : \boldsymbol{T}^p) \rangle_V$ is negative over the whole range of time when $W_i = 1$, meaning that this term inhibits the enstrophy production. This is also consistent with the DNS result obtained using the FENE-P model with $W_i < 1$ (Cai *et al.* 2010). While for $W_i = 5$ and 25, this term is positive and attains a maximum value at around $t^* = 5$, and decays for $t^* > 5$. Thus, the term $\langle (\nabla \times \boldsymbol{\omega}) \cdot (\nabla : \boldsymbol{T}^p) \rangle_V$ contributes to the vorticity production in (4.8) when W_i is larger. Interestingly, the growth of the enstrophy production by the polymer stress when W_i increases is offset by a corresponding decrease of the enstrophy dissipation $-\nu_s \langle (\nabla \boldsymbol{\omega})^2 \rangle_V$ when W_i increases, as shown in figure 16(*c*). Figure 16(*d*) also shows that, for $t^* > 2$, dE_ω/dt is

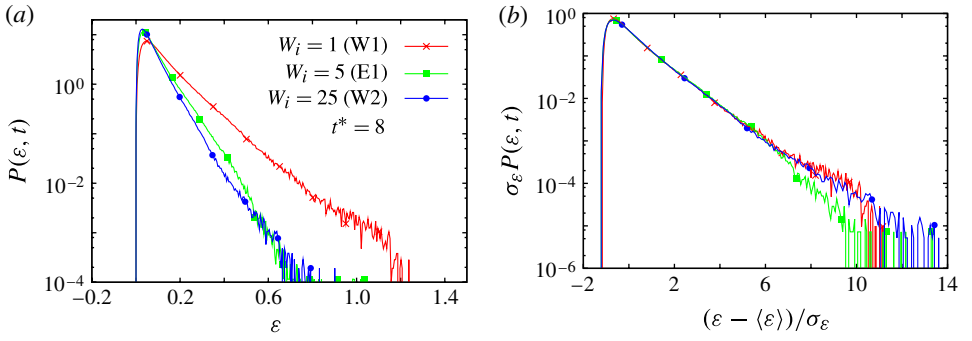

FIGURE 17. (Colour online) Comparison of the p.d.f. behaviour for fluctuations of the local energy dissipation rate $\tilde{\varepsilon}(\boldsymbol{x}, t)$ for various W_i using (*a*) bare variables and (*b*) normalized variables.

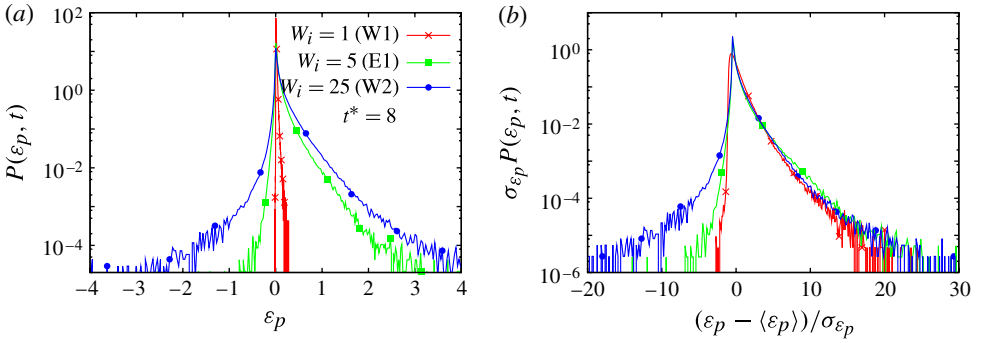

FIGURE 18. (Colour online) Comparison of the p.d.f. behaviour for fluctuations of the local production/inhibition rate $\tilde{\varepsilon}_p(\boldsymbol{x}, t)$ of the kinetic energy due to the polymer stress for various W_i using (*a*) bare variables and (*b*) normalized variables.

negative, and its amplitude gradually increases with W_i, indicating enstrophy inhibition when $t^* > 2$. These observations suggest that the modification of the decay rate of enstrophy (or, alternatively, the energy dissipation rate) by polymer additives is mostly due to the growth of the amplitudes of both $\langle(\boldsymbol{\nabla} \times \boldsymbol{\omega}) \cdot (\boldsymbol{\nabla} : \boldsymbol{T}^p)\rangle_V$ and $-\nu_s \langle(\boldsymbol{\nabla}\boldsymbol{\omega})^2\rangle_V$ when W_i increases. An important finding is that the role of $\langle(\boldsymbol{\nabla} \times \boldsymbol{\omega}) \cdot (\boldsymbol{\nabla} : \boldsymbol{T}^p)\rangle_V$ for the enstrophy production/inhibition changes with W_i, where this term works as an enstrophy inhibitor in the lower W_i case. We infer that this nature is related to the details of the coil–stretch transition of the ensemble of dumbbells which is observed at around $W_i = 4$ (Watanabe & Gotoh 2010).

We next consider the Weissenberg number's effects on the p.d.f. behaviour of $\tilde{\varepsilon}$ and $\tilde{\varepsilon}_p$ for various W_i. The results are presented in figures 17 and 18, respectively. The probability of finding a large value of $\tilde{\varepsilon}$ decreases as W_i increases, indicating a stronger energy dissipation reduction for larger W_i. However, the p.d.f. form for the normalized variable is almost identical irrespective of W_i for $(\varepsilon - \langle\varepsilon\rangle)/\sigma_\varepsilon < 6$, similar to the result in figure 6(*b*). Berti *et al.* (2006) observed a collapse of the normalized p.d.f. curves of the fluid acceleration over the entire intensity of fluctuations for various W_i by using the simplified viscoelastic fluid model. If the Kolmogorov

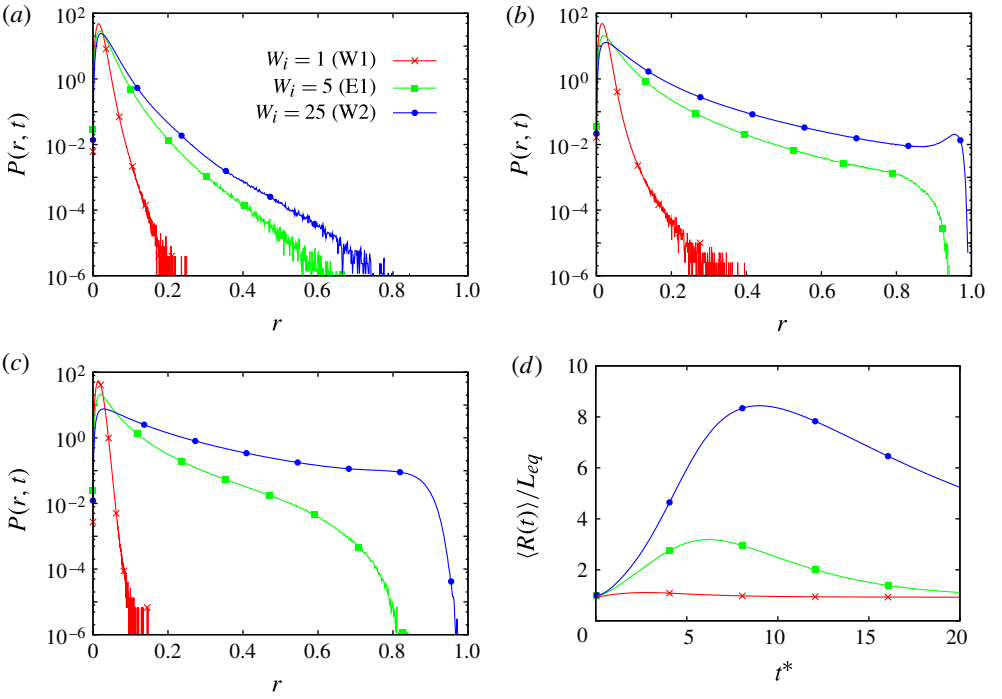

FIGURE 19. (Colour online) Effect of W_i on the temporal evolution of the polymer extension p.d.f. $P(r, t)$ normalized by the maximum extension length L_{max} for (*a*) $t^* = 2$, (*b*) $t^* = 4$ and (*c*) $t^* = 8$ and (*d*) the temporal evolutions of the mean dumbbell extension $\langle |\boldsymbol{R}^{(n)}| \rangle$ divided by $L_{eq} = \sqrt{3} r_{eq}$.

scaling is applied to the fluid acceleration $\boldsymbol{a}$, $|\boldsymbol{a}| \sim (\tilde{\varepsilon}^3/\nu_s)^{1/4}$ holds, implying that the statistical nature of $|\boldsymbol{a}|$ is closely related to that of $\tilde{\varepsilon}$. This suggests that the present result is consistent with that by Berti *et al.* (2006). The p.d.f. tails for $\tilde{\varepsilon}_p$ in figure 18(*a*) spread wider for larger W_i. Figure 18(*b*) also shows that the probability of observing a negative value of $\tilde{\varepsilon}_p$ increases with W_i, even when normalized by their standard deviation. This indicates the existence of a larger reaction of the ensemble of dumbbells to the fluid motions when W_i is larger. The p.d.f. curves for the positive value of $\tilde{\varepsilon}_p$ are almost overlaid on the same curve once the p.d.f.s are normalized.

Comparisons of the p.d.f. behaviour for the end-to-end distance of dumbbells for various W_i are shown in figure 19 for (*a*) $t^* = 2$, (*b*) $t^* = 4$ and (*c*) $t^* = 8$. The p.d.f. tail is longer with increasing W_i for every time considered. For $W_i = 25$ at $t^* = 4$, there are a large number of dumbbells with stretched configurations close to L_{max}. In the decay regime of $\varepsilon(t)$ ($t^* > 4$), the fully stretched dumbbells shrink toward their equilibrium states. This is clearly shown in figure 19(*d*), where the temporal evolutions of the mean end-to-end distance of the dumbbells normalized by L_{eq} are plotted for various W_i. The mean dumbbell extension for $W_i = 1$ remains nearly L_{eq} for the entire time, indicating that there is no significant back reaction to the fluid motion. For $W_i = 25$, the mean extension sharply increases until $t^* = 8$, and then gradually decays for $t^* > 8$. A similar trend is observed in the behaviour of $U(t)$, as seen in figure 14(*a*).

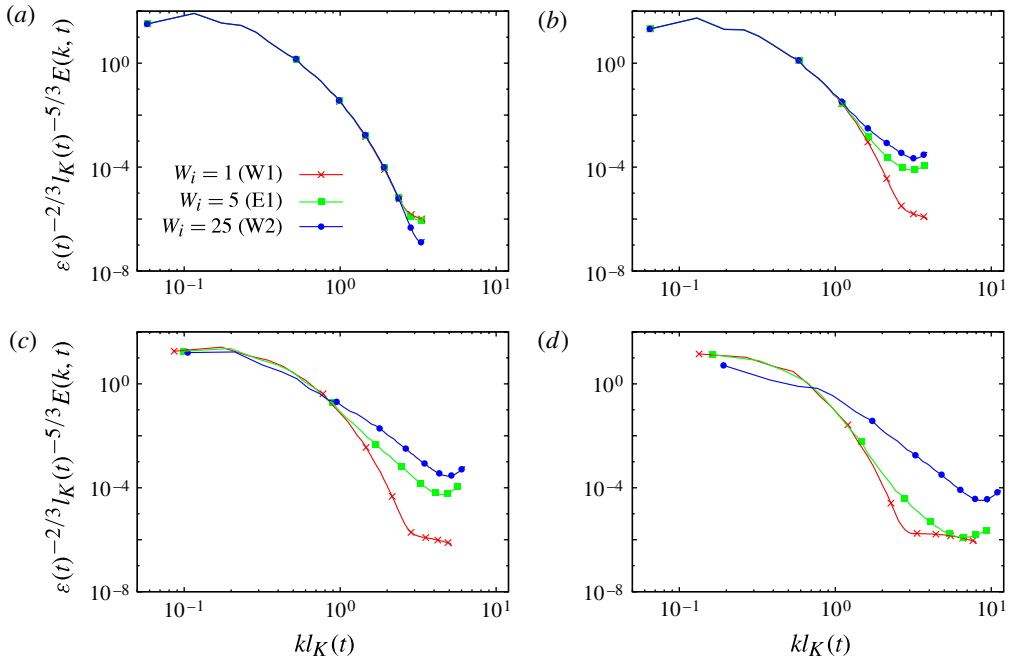

FIGURE 20. (Colour online) Comparison of the kinetic energy spectrum $E(k, t)$ normalized using the Kolmogorov scaling for Runs W1, E1 and W2 for (*a*) $t^* = 2$, (*b*) $t^* = 4$, (*c*) $t^* = 8$ and (*d*) $t^* = 16$.

Because the relaxation time τ is proportional to W_i under a fixed flow condition, there are many dumbbells with stretched configurations for larger W_i, even when the turbulence decays. The stretched dumbbells contribute to an increase in the polymer stress field, leading to strong modifications not only in the dynamics in physical space but also in the spectral dynamics. It is interesting to investigate how the polymer effect is distributed over a wide range of length scales, and how the spectral dynamics depends on W_i. We first investigate the effects of the Weissenberg number on the spectral behaviour by comparing the kinetic energy spectrum $E(k, t)$ for various values of W_i. Figure 20 presents the resulting curves for (*a*) $t^* = 2$, (*b*) $t^* = 4$, (*c*) $t^* = 8$ and (*d*) $t^* = 16$ normalized by the Kolmogorov scaling (5.1). The curves for $t^* = 2$ and 4 collapse onto a single curve, irrespective of W_i except for their spectral tails. The collapsing region observed at $t^* = 4$ becomes narrower than for $t^* = 2$, indicating that the equilibrium range described in Kolmogorov theory shrinks as the time progresses. Unlike the case for the η-dependence, the normalized spectrum does not collapse for later times, even for smaller wavenumbers, and the deviation of the curve for $W_i = 25$ from the others is remarkable. It should be noted that the W_i dependence of the spectral behaviour at the later times is similar to the DNS results of the FENE-P model with isotropic steady turbulence (Perlekar *et al.* 2010). A DNS study using the FENE-P model by Angelis *et al.* (2005) examined the behaviour of the second-order structure function in the steady isotropic turbulence with polymer additives by varying the Deborah number D_e (corresponding to W_i). They observed that the fluctuations depleted at small-scales, but increased at large ones when D_e increased. This observation is at variance with the results of the present case. We think that the

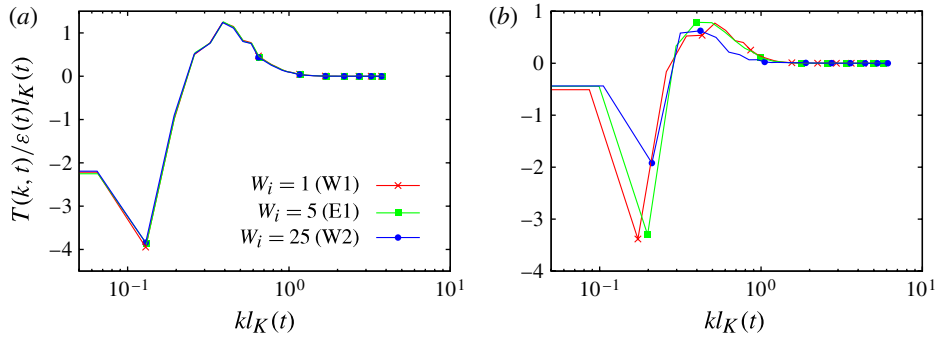

FIGURE 21. (Colour online) Energy transfer function $T(k, t)$ normalized by $\varepsilon(t)l_K(t)$ against $kl_k(t)$ for various W_i: (*a*) $t^* = 4$; and (*b*) $t^* = 8$.

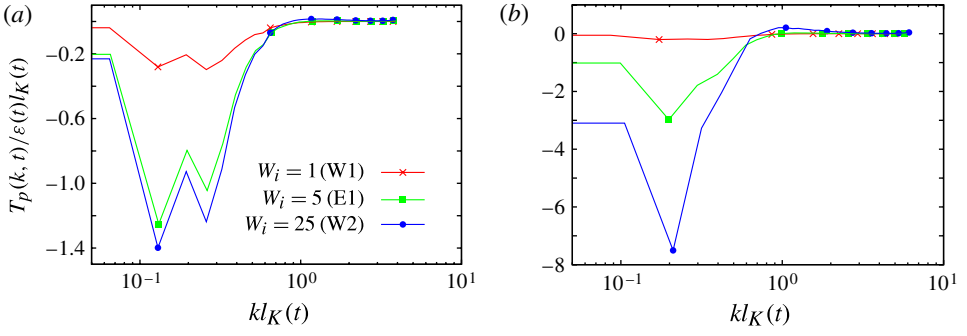

FIGURE 22. (Colour online) Polymer contribution to the energy transfer $T_p(k, t)$ normalized by $\varepsilon(t)l_K(t)$ against $kl_k(t)$ for various W_i: (*a*) $t^* = 4$; and (*b*) $t^* = 8$.

effect of polymer additives on the statistics might be dependent on the details of the large-scale natures such as whether the forcing mechanism exists. This calls for further investigations for the case of steady turbulence with polymer additives using the hybrid approach, which is a future subject of this study.

Figure 21 compares the curves for the energy transfer flux $T(k, t)$ normalized by $\varepsilon(t)l_K(t)$ ($\hat{T}(k, t) \equiv T(k, t)/\varepsilon(t)l_K(t)$) for (*a*) $t^* = 4$ and (*b*) $t^* = 8$. The results of $\hat{T}(k, t)$ collapse onto a single curve for $t^* = 4$, corresponding to the spectral collapse shown in figure 20(*b*) and indicating that the polymer effects are not significant for $t^* \leqslant 4$. However, for $t^* = 8$, the amplitude of $\hat{T}(k, t)$ for $kl_K(t) < 0.3$ decreases as W_i increases. Thus, the suppression of the energy transfer rate by polymer additives increases with W_i.

The contributions of the dumbbell dynamics to the spectral equation are examined by investigating the behaviour of $\hat{T}_p(k, t) \equiv T_p(k, t)/\varepsilon(t)l_K(t)$, which is plotted in figure 22. $\hat{T}_p(k, t)$ is negative for wavenumbers below $l_K(t)$ at both $t^* = 4$ and 8. In addition, as W_i increases, the amplitude of $\hat{T}_p(k, t)$ increases over the same wavenumber range. Thus, the decrease of kinetic fluid energy by $T_p(k, t)$ becomes more significant for larger W_i at small wavenumbers. As shown in figure 22(*b*), $T_p(k, t)$ of $W_i = 25$ at $t^* = 8$ for wavenumbers $kl_K(t) > 1$ is positive. This indicates

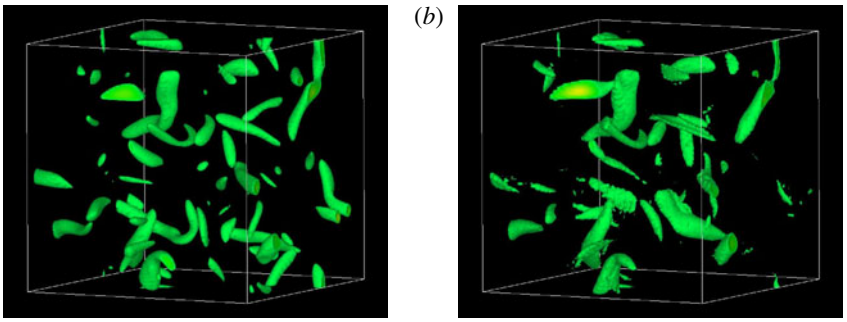

FIGURE 23. (Colour online) Comparison of the iso-surface of Q for the one-way case (*a*: Run A) and $\eta = 0.1045$ (*b*: Run E1) for $t^* = 7$. The iso-surface level is chosen by $Q/Q_{rms} = 3$ for both cases.

that there is an energy source below the Kolmogorov length scale, implying that the spectral dynamics in the far dissipation range for $W_i = 25$ is significantly different from the other values of W_i used here. This is seen in the behaviour of the energy spectrum for $W_i = 25$, showing a power-law decay for wavenumbers $kl_K(t) > 1$. This point will be discussed in a later section.

Based on the data and results discussed above, we conclude that polymers having larger values of W_i are more efficient reducers of turbulence at both large and small scales. These results are qualitatively consistent with the results of DNSs obtained using the FENE-P model (Perlekar *et al.* 2010).

5.3. *Effects on coherent structures*

By examining the modification of coherent structures, we can understand the role of polymer additives on the turbulent flow.

Figure 23 compares the vortical structures obtained for Run A (one-way) and Run E1 (two-way) at $t^* = 7$. These are iso-surfaces of the second invariant Q of the velocity gradient tensor $\nabla \boldsymbol{u}$. Although the structures are generally indistinguishable from each other, the generation of intense structures is suppressed more in the two-way case (Run E1) than in the one-way case (Run A). Moreover, the width of the vortex tube with polymer additives increases slightly in the two-way case, although the length remains unchanged, consistent with the reduction of energy dissipation observed in figures 2 and 6 and the results of DNS studies using the FENE-P equation (Perlekar *et al.* 2006, 2010; Cai *et al.* 2010).

Another interesting property is the spatial distribution of the stretched dumbbells, and how this distribution is related to the vortical structures. To this end, we investigate the field structure of the trace of the polymer stress tensor $T^p_{ii}(\boldsymbol{x})$. Figure 24 depicts the iso-surface of T^p_{ii} obtained for Run E2 at $t^* = 7$ for the two cases of iso-surface level. It is recognized that peculiar sheet-like structures are found within the regions of intermediate intensity fluctuation, while regions with larger values of T^p_{ii} contain filament-like structures. This suggests that the characteristic structure in T^p_{ii} depends on the intensity of the fluctuations. Sheet-like structures are clearly visible in figure 25(*a*), which shows a two-dimensional (2D) slice of figure 24. We confirm that the contour length of a slice of a sheet is about the order of the integral scale L, while the width of the sheet is about the order of l_K. This organized structure is due to the existence of collective motion of the stretched dumbbells whose dynamics strongly correlates with the Lagrangian dynamics of the local velocity gradient. Because the

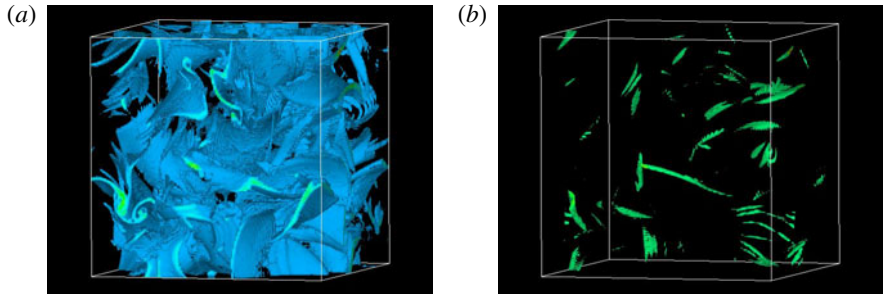

FIGURE 24. (Colour online) Iso-surface of the trace of the polymer stress tensor $X = T^p_{ii}$ obtained for Run E2 for $t^* = 7$. The iso-surface level is chosen by $X/X_{rms} = 1.5$ (a) and $X/X_{rms} = 6$ (b).

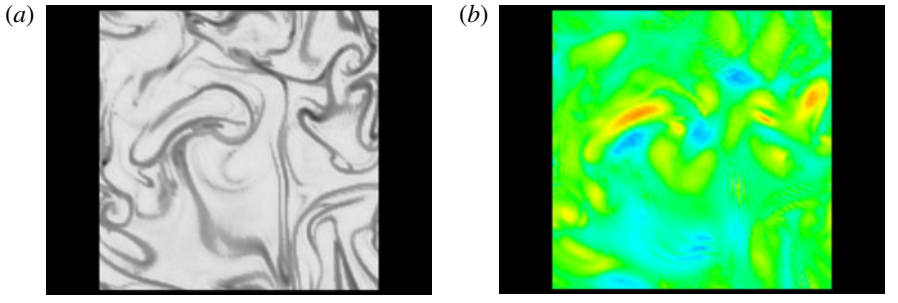

FIGURE 25. (Colour online) Comparison between the 2D slices of T^p_{ii} (a) and Q (b) obtained for Run E2 for $t^* = 7$.

velocity gradient field has a coherent vortical structure with a wide range of scales, it is reasonable to conclude that the polymer–turbulence interaction leads to the large-scale structures in T^p_{ii}, as observed in figures 24 and 25(a). This also suggests that T^p_{ii} has spectral support in the range of both large and small wavenumbers. Thus, the polymer additives can affect the large-scale turbulent motions, as seen in figures 11 and 22 even when the size of polymer itself is smaller than l_K.

When the sheet-like structures in T^p_{ii} are compared with the structures in Q shown in figure 25(b), the stretched dumbbells congregate among intense regions of positive Q values. This is reminiscent of the sheet-like structures observed in the scalar gradient field of the passive scalar turbulence (Brethouwer, Hunt & Nieuwstadt 2003; Schumacher, Sreenivasan & Yeung 2005; Gotoh & Watanabe 2012). In fact, the amplification mechanism of the scalar gradient vector is similar to that of the end-to-end vector for a dumbbell. Further analysis is needed to understand the relationship between the nature of the velocity gradient tensor and the end-to-end vector of the dumbbells and their η and W_i dependencies.

6. Validation for evaluating the polymer stress field

In § 2.2, we discussed that it is indispensable to assume the existence of many replica dumbbells in the flow because of the limitation of computational resources even when a state-of-the-art supercomputer is used. To assess the validity of the

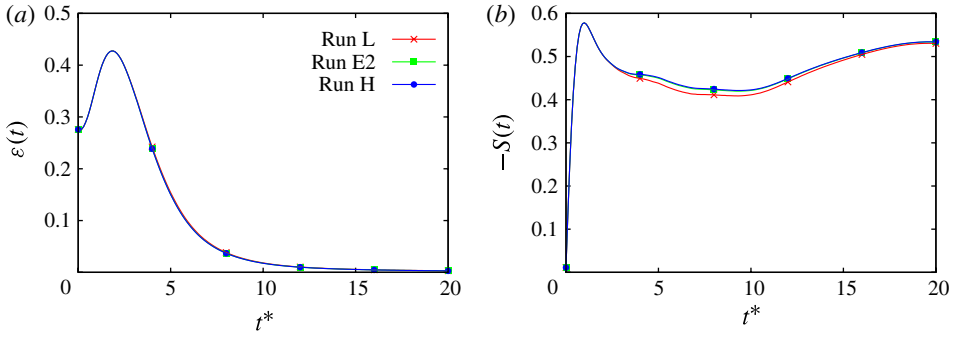

FIGURE 26. (Colour online) Effect of the number of dumbbells on the temporal evolution of (*a*) the energy dissipation rate $\varepsilon(t)$ and (*b*) the skewness factor $S(t)$ for the longitudinal velocity derivative. Note that the curves for Runs E2 and H in (*b*) collapse onto each other.

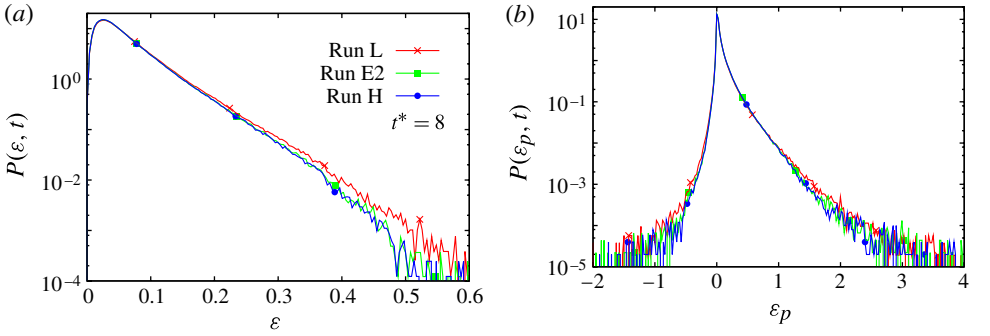

FIGURE 27. (Colour online) Effect of the number of dumbbells on the p.d.f. behaviour of (*a*) the local energy dissipation rate $\tilde{\varepsilon}$ and (*b*) the local production/inhibition rate $\tilde{\varepsilon}_p$ at $t^* = 8$.

introduced assumption, it is necessary to know the minimum number of dumbbells that is required to adequately reproduce the experimental results. For this, we examine the effects of the variation of b and $\tilde{N}_t$ on the present results under fixed physical conditions such as N_t.

A comparison of the temporal evolution of $\varepsilon(t)$ and $-S(t)$ for Runs L, E2 and H is shown in figure 26. Here Run L (Run H) was performed by using the smaller (larger) numbers of $\tilde{N}_t$ and $1/b$ than those for Run E2 with fixed $b\tilde{N}_t$. The temporal evolution of both quantities is almost indistinguishable among the three runs, although there is a very small deviation in the $-S(t)$ curve of Run L from the others in the range $3 < t^* < 15$. The skewness factor is the higher-order statistics of the velocity gradient that is largely dependent on the degree of computational accuracy in evaluating the polymer stress field. Figure 27 compares the p.d.f. curves for (*a*) $\tilde{\varepsilon}$ and (*b*) $\tilde{\varepsilon}_p$ obtained at $t^* = 8$. The p.d.f. curves of both $\tilde{\varepsilon}$ and $\tilde{\varepsilon}_p$ at around the most probable part collapse among the three runs. While the probability of finding intense values of $\tilde{\varepsilon}$ in Run L is larger than in the other runs, indicating an over-estimation of the energy dissipation fluctuation at large magnitudes. A similar trend can be seen for $\tilde{\varepsilon}_p$.

To observe the effects of the parameters on the turbulence statistics in more detail, we also compare the behaviour of the spectra $k^2E(k, t)$ at several time steps

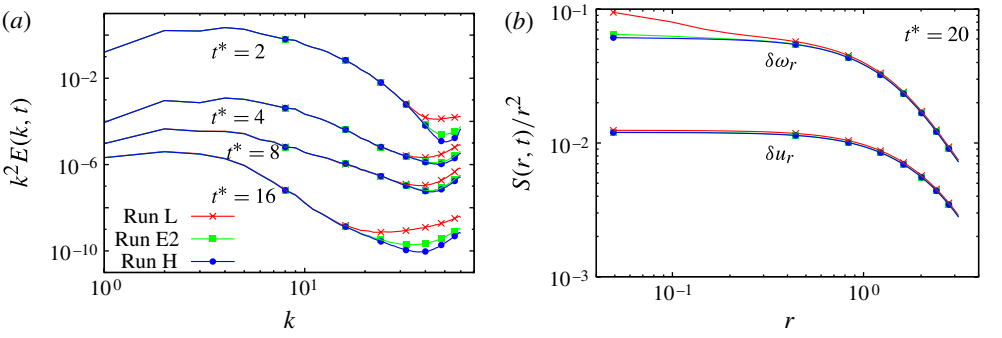

FIGURE 28. (Colour online) (*a*) Comparison of the time evolution of $k^2E(k,t)$ for Runs L, E2 and H. The curves for $t^* = 4$, 8 and 16 are shifted downward by multiplying by the appropriate numerical factor. (*b*) Comparison of the behaviour of the second-order longitudinal velocity and vorticity structure functions at $t^* = 16$. The structure function is plotted by dividing by r^2 to examine the analyticity at small scales.

in figure 28(*a*). The spectral behaviour is indistinguishable except near the cutoff wavenumbers when $t^* < 8$. However, Run L has a large deviation from the others at $t^* = 16$ for high wavenumbers, which may be attributed to an insufficient number of dumbbells in our calculation to obtain smooth variations of $\boldsymbol{T}^p$ at the grid scale.

The raised spectra at high wavenumbers observed in Run L compared with Run H suggests that the variations of the velocity and velocity gradient fields might not be smooth enough. To examine this point, we evaluate the behaviour of structure functions for the longitudinal velocity and vorticity differences, which are defined by

$$S_q^u(r,t) = \langle(\delta u_r)^q\rangle_V, \quad S_q^\omega(r,t) = \langle(\delta\omega_r)^q\rangle_V\,. \tag{6.1}$$

Here, $\delta u_r = (\boldsymbol{u}(\boldsymbol{x}+r,t)-\boldsymbol{u}(\boldsymbol{x},t))\cdot\boldsymbol{r}/r$ and $\delta\omega_r = (\boldsymbol{\omega}(\boldsymbol{x}+r,t)-\boldsymbol{\omega}(\boldsymbol{x},t))\cdot\boldsymbol{r}/r$. The structure functions must be analytic at small scales, i.e. they must behave as $S_q^u(r,t) \sim r^q$ and $S_q^\omega(r,t) \sim r^q$ in the limit $r \to 0$. The resulting curves in figure 28(*b*) for $q = 2$ are plotted by compensating for the r^2 behaviour at small scales. We confirm that $S_2^u(r,t) \sim r^2$ at small scales, irrespective of $\tilde{N}_t$, but the curve of $S_2^\omega(r,t)$ for Run L deviates from the others. These results indicate that although the velocity field is well resolved for a small number of dumbbells, a greater number of dumbbells (at least $> 10^9$ in the present case) is actually required to resolve the velocity gradient field at small scales.

Figure 29 compares the coherent vortices obtained for Run L to those for Run H by using the iso-surface of the positive region of Q. Zig-zag structures are observed in the surfaces of vortices for Run L, unlike Run H, although the vortex structures for both runs are quite similar to each other. These zig-zag structures correspond to the spectral rise observed in Run L (figure 28*a*).

These results suggest that the replica assumption introduced to evaluate $\boldsymbol{T}^p$ is valid when discussing the large-scale nature of turbulence, but a much larger number of dumbbells is required for better resolution of the turbulence modifications below the Kolmogorov length scale.

Finally we examine the resolution effects on the evaluation of the polymer stress tensor $T_{ij}^p(\boldsymbol{x},t)$. Here $T_{ij}^p(\boldsymbol{x},t)$ is evaluated by (2.10) with the approximations (3.9) and (3.10) and hence the polymer stress field constructed from the Lagrangian dumbbell dynamics depends on the grid spacing Δx. Generally speaking, a finer

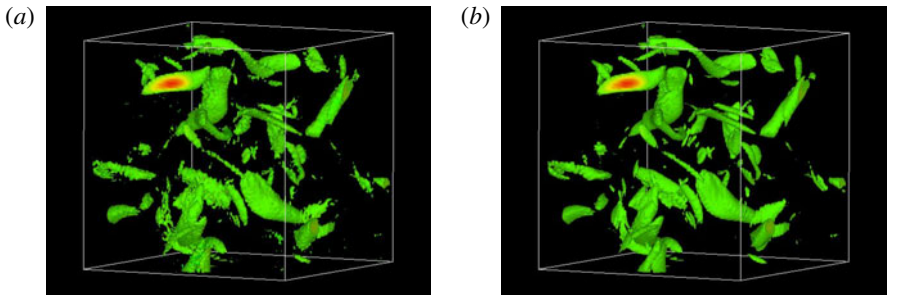

FIGURE 29. (Colour online) Comparison of iso-surface visualizations of vortical structures using Q with $Q/Q_{rms} = 2.5$ (a: Run L; b: Run H) at $t^* = 7$.

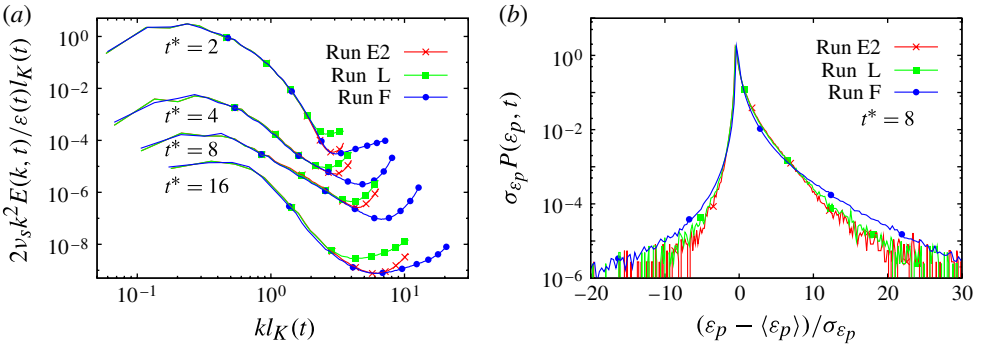

FIGURE 30. (Colour online) Examination of the resolution effects on the turbulence statistics: (a) time evolutions of the energy dissipation spectra normalized by Kolmogorov scaling; and (b) normalized p.d.f.s for the fluctuations of $\tilde{\varepsilon}_p$ at $t^* = 8$. The curves for $t^* = 4$, 8 and 16 in (a) are shifted downward by multiplying by the appropriate numerical factor.

spatial resolution leads to a more accurate evaluation of $T_{ij}^p(\boldsymbol{x}, t)$. To test this point, we performed an additional DNS (Run F) with the same numerical and physical conditions as Run E2 except for the spatial resolution, where Run F was performed with $N^3 = 256^3$. Here we can discuss the resolution effects on the evaluation of $T_{ij}^p(\boldsymbol{x}, t)$ from two viewpoints. The first point is to compare Run F to Run E2, which gives only information about the degree of accuracy by changing Δx. The second point is to compare Run F with the results of Run L, which has a smaller number of dumbbells. However, the mean number of dumbbells per unit cell ($\tilde{N}_t/\Delta x^3$) of the Eulerian computation for Run F is the same as that for Run L, meaning that the degree of statistical convergence in constructing $T_{ij}^p(\boldsymbol{x}, t)$ at each grid point can be regarded as being identical for both cases.

Figure 30(a) shows a comparison of the temporal evolutions of the normalized dissipation spectra $2\nu_s k^2 E(k,t)/\varepsilon(t) l_K(t)$ obtained for Runs E2, L and F. At $t^* = 2$ and 16, the wavenumber at which the spectra start to rise is almost the same for both Run E2 and F, indicating that there is little effect on the accuracy of computation by changing Δx. This is due to the fact that the polymer effects are not important up to $t^* = 2$, and that the turbulence adequately decays up to $t^* = 16$, where the DNS condition is satisfied irrespective of Δx. However, we can confirm that the spectral

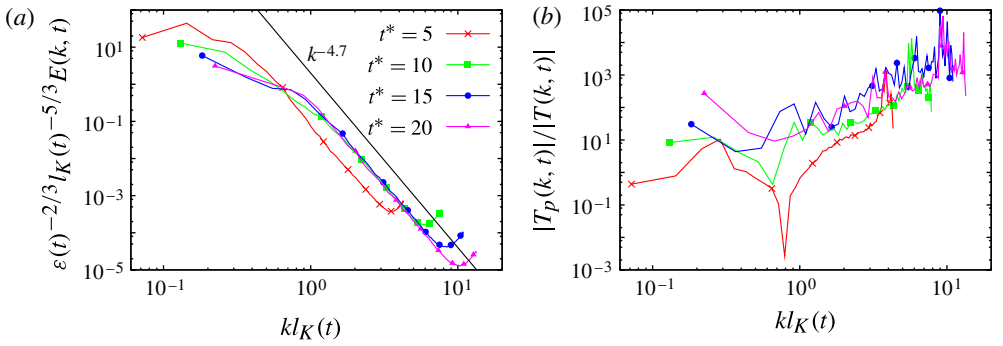

FIGURE 31. (Colour online) Temporal evolution of (*a*) the kinetic energy spectrum $E(k, t)$ normalized by the Kolmogorov unit and (*b*) the ratio of the absolute value of the transfer functions defined by $|T_p(k, t)|/|T(k, t)|$ for Run W2 ($W_i = 25$).

tails obtained for Run F mildly extend toward the larger wavenumbers at $t^* = 4$ and 8 when compared with Runs E2 and L. This suggests that we need finer spatial resolution to get better statistics at small-scales. The comparison of the normalized p.d.f.s for $\tilde{\varepsilon}_p$ obtained for Runs E2, L and F are shown in figure 30(*b*). Although the probability of finding weak fluctuation intensity is insensitive to the variation of Δx, the rare fluctuations obtained in Run F have a larger probability than the other runs. This might be due to an insufficient resolution for resolving intermittent fluctuations of T_{ij}^p (as seen in figures 24 and 25), which is also similar to the observations in the p.d.f. behaviour of the derivative field obtained by passive scalar DNS with several resolution conditions (Watanabe & Gotoh 2007).

The above results imply that the resolution effects are significant for the small-scale nature of turbulence in addition to the effect of the variation of the number of replica dumbbells when the turbulence is developing. Moreover, we can confidently conclude that the approximation (3.9) and (3.10) for evaluating $T_{ij}^p(\boldsymbol{x}, t)$ works satisfactorily irrespective of Δx used here ($N^3 = 128^3$ or 256^3).

7. Discussion

7.1. *Power-law spectrum for higher W_i*

In this section, we discuss the spectral behaviour obtained from Run W2 ($W_i = 25$). Note that in figure 20(*d*), the spectral behaviour at $t^* = 16$ for $W_i = 1$ is different from that for $W_i = 25$. At $t^* = 16$, the curve for $W_i = 25$ has a near power-law decay. To examine this behaviour in more detail, the temporal evolution of $E(k, t)$ for Run W2 is shown in figure 31(*a*), using dimensionless variables. We can clearly confirm a scaling law close to $E(k) \propto k^{-4.7}$ for high wavenumbers when $t^* \geqslant 10$, and the scaling range includes smaller-scales as time progresses. Figure 31(*b*) demonstrates the behaviour of the ratio $|T_p(k, t)|/|T(k, t)|$ defined using the transfer functions. Although there are large variations of data in the high wavenumber range because $T(k, t)$ and $T_p(k, t)$ are not definitely positive, it is confirmed that $|T_p(k, t)| \gg |T(k, t)|$ for $kl_k(t) > 1$. It should be emphasized that the energy transfer due to the nonlinear advection term is not important in forming the power-law spectrum shown in figure 31(*a*). This implies that the spectral dynamics of the velocity field are dominated by the simple balance equation $\nu_s \nabla^2 \boldsymbol{u} = -\nabla : \boldsymbol{T}^p$.

We now discuss the relationship between the present power-law spectrum and the elastic turbulence. Elastic turbulence, which is characterized by $R_e = O(1)$ and $W_i = O(10)$, shows a power-law decay in the kinetic energy spectrum $E(k) \propto k^{-\theta}$ for a swirling flow between two parallel discs with $\theta = 3.5$ (Groisman & Steinberg 2000; Burghelea *et al.* 2007) and $\theta = 3.8$ (Berti *et al.* 2008) in DNS studies of the Oldroyd-B model with 2D Kolmogorov flow. The scaling exponent in the cited works is not as large as the value $\theta = 4.7$ calculated here for Run W2 at $t^* = 20$ (figure 31*a*), although our result is consistent with theoretical predictions for $\theta > 3$ (Fouxon & Lebedev 2003). The instantaneous Reynolds and Weissenberg numbers defined using the value of $\varepsilon(t^*)$, are respectively obtained to be $R_\lambda^* = 3.5$ and $W_i^* = 1.7$ for Run W2 at $t^* = 20$. Thus, our work uses a larger R_λ and smaller W_i than those used in the preceding studies. An investigation into the origin of the scaling behaviour of $E(k)$ by performing a DNS of a smaller R_λ case under a statistically steady state is the subject of future work.

7.2. *Robustness of the normalized p.d.f. form*

It is difficult to clarify the physical mechanism behind the robustness of the normalized p.d.f. form of $\tilde{\varepsilon}$ under variations of the parameters η and W_i, which is shown in figures 6(*b*) and 17(*b*). Here we speculate a scenario explaining this observation.

The multi-fractal theory for the energy dissipation intermittency (Frisch 1995) expresses $\tilde{\varepsilon}$ as

$$\tilde{\varepsilon} \sim \varepsilon_L \left(\frac{l_K}{L}\right)^{\alpha_n - 1}, \tag{7.1}$$

where $\alpha_n(\boldsymbol{x}, t)$ is the singularity exponent which fluctuates in space and time, and ε_L is the energy dissipation at the integral scale L, being dependent on η and W_i. The statistical nature of $\tilde{\varepsilon}$ depends on ε_L, l_K/L, and the statistics of α_n. If we consider the effect of polymer additives on the energy dissipation fluctuations in this framework, (7.1) should be extended to

$$\tilde{\varepsilon} \sim \varepsilon_L \left(\frac{l_L}{L}\right)^{\alpha_n - 1} \left(\frac{l_K}{l_L}\right)^{\alpha_p - 1}, \tag{7.2}$$

where $\alpha_p(\boldsymbol{x}, t)$ is also the singularity exponent characterizing the effect of polymer additives in the scale below $l_L (> l_K)$. If the polymer additives do not modify the statistics of α_n, i.e. if α_p is statistically independent of α_n, we obtain the qth-order moment of $\tilde{\varepsilon}$ in the form

$$\frac{\langle \tilde{\varepsilon}^q \rangle}{\varepsilon_L^q} \sim \left(\frac{l_L}{L}\right)^{\tau_n(q)} \left(\frac{l_K}{l_L}\right)^{\tau_p(q)}, \tag{7.3}$$

where $\tau_n(q)$ and $\tau_p(q)$ are respectively the qth-order intermittency exponents corresponding to α_n and α_p. Moreover, if the probability of finding the singularity in $\tilde{\varepsilon}$ is not modified by polymer additives, we expect that the statistical nature of α_p is close to that of α_n, meaning that $\tau_n(q) \simeq \tau_p(q)$. We thus have the relationship

$$\frac{\langle \tilde{\varepsilon}^q \rangle}{\varepsilon_L^q} \sim \left(\frac{l_K}{L}\right)^{\tau_n(q)}. \tag{7.4}$$

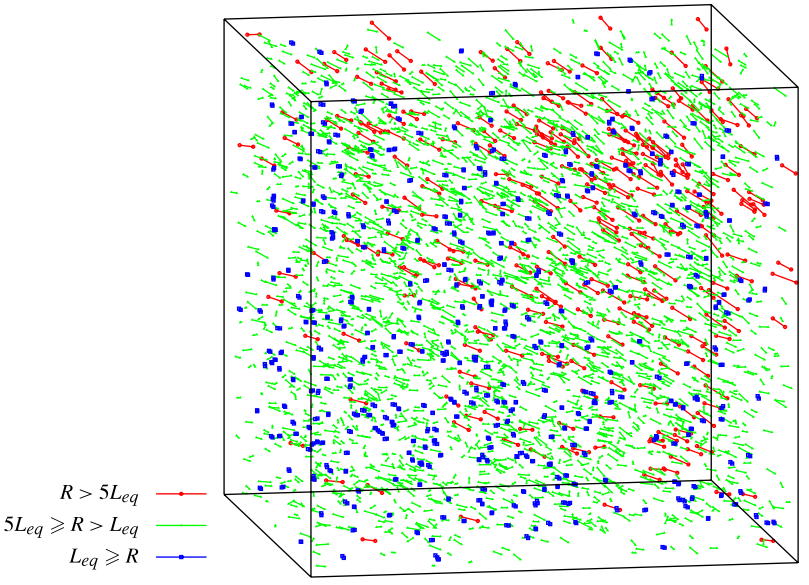

FIGURE 32. (Colour online) Dumbbell configurations within a unit cell Δx^3 centred at the origin obtained for Run H at $t^* = 7$. The colour of line indicates the dumbbell's extension length categorized into three cases as $|\boldsymbol{R}^{(n)}| > 5L_{eq}$ (red online), $5L_{eq} \geqslant |\boldsymbol{R}^{(n)}| > L_{eq}$ (green online) and $L_{eq} \geqslant |\boldsymbol{R}^{(n)}|$ (blue online). There are 3626 dumbbells located within this box.

As shown in figures 4(*b*) and 15(*b*), the scale ratio l_K/L is insensitive to variation in η and W_i, suggesting also that $\langle\tilde{\varepsilon}^q\rangle/\varepsilon_L^q$. Thus, the statistics of $\tilde{\varepsilon}/\varepsilon_L$ are not greatly affected by the polymer additives.

The above scenario is fairly speculative and depends on unresolved assumptions. It is important for future studies to examine its validity.

7.3. *Replica assumption*

The success of the replica assumption implies that all of the dumbbells contributing to the polymer stress tensor at a single grid point have similar stretched configurations. To explore this implication further, we investigate the dumbbell configurations within a unit cell of Δx^3 centred around the origin of the computational box. Figure 32 illustrates the resulting dumbbell configurations obtained for Run H, where the dumbbells are represented by solid lines of three different colours. We can confirm that there are a few stretched dumbbells within this unit cell, and that they have similar orientations. To observe the second point in more detail, we generate a scatter plot characterizing the dumbbell configurations. We define the angles $\theta^{(n)}$ and $\phi^{(n)}$ by

$$\theta^{(n)} \equiv \cos^{-1}\left(\frac{R_3^{(n)}}{|\boldsymbol{R}^{(n)}|}\right), \tag{7.5}$$

$$\phi^{(n)} \equiv \tan^{-1}\left(\frac{R_2^{(n)}}{R_1^{(n)}}\right). \tag{7.6}$$

Figure 33 shows the resulting plot representing the dumbbells' extension and orientation in the θ–ϕ plane using the data from figure 32. Here, the colour of

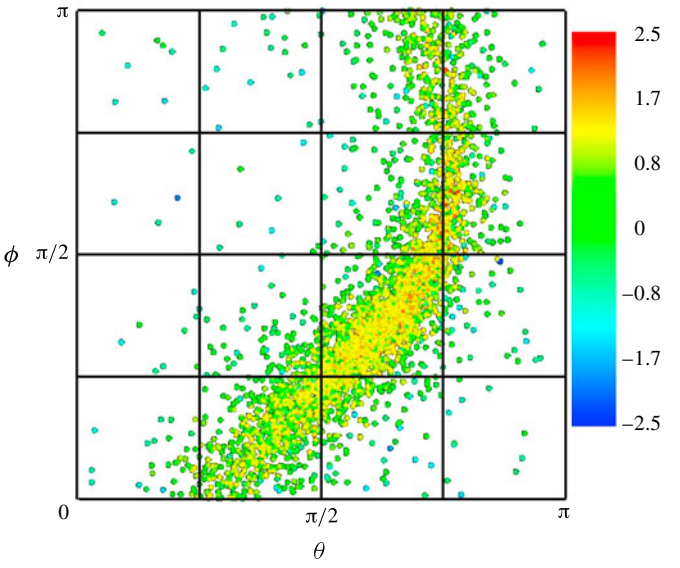

FIGURE 33. (Colour online) Scatter plot of the dumbbell orientations in the θ–ϕ plane using the data of figure 32. The colour of each point indicates the value of the logarithm of the normalized dumbbell extension $\ln(R^{(n)}/L_{eq})$.

each point indicates the value of the dumbbell extension defined by $\ln(|\boldsymbol{R}^{(n)}|/L_{eq})$. The plotting range of ϕ was limited within $0 \leqslant \phi \leqslant \pi$ because the dumbbell configuration with $-\boldsymbol{R}^{(n)}$ is regarded as being the same as that for $\boldsymbol{R}^{(n)}$. It is recognized that the points representing the dumbbell length larger than L_{eq} are localized in the region around $(\theta, \phi) = (3\pi/4, \pi/2)$, indicating that the stretched dumbbells have similar orientations. While the dumbbells with extensions below L_{eq} are distributed over the θ–ϕ plane, suggesting that the orientation is random for unstretched dumbbells. The specific structure of this localized region may be attributed to the structure of the local flow topology at the considered spatial point. Further study is needed to clarify the detailed relationship between the dumbbell orientations and the principal axis of the rate of strain tensor.

A recent theoretical study suggests that the end-to-end vectors of polymers within the fluid blob (scale l_K) are synchronized by the flow with W_i above the coil–stretch transition even when they have initially random directions (Fouxon & Posch 2012). Figure 33 seems to support this idea, and the existence of synchronization may be a strong theoretical foundation for justifying the replica assumption used in the present hybrid simulation.

In the statistical sense, because the stretched dumbbells make a significant contribution to the polymer stress tensor, it is important to disperse a large number of dumbbells in the flow to accurately describe T_{ij}^p when using (2.10). If the number of polymers is insufficient, there will be very few stretched dumbbells per unit cell, leading to poor statistical convergence of T_{ij}^p at the grid scale. This is the origin of the undesirable behaviour at small scales observed in figures 28 and 29.

8. Conclusions

Parallel computations of turbulent polymer solution flow were performed using a hybrid approach consisting of a Brownian dynamics simulation for a polymer model

(dumbbell) and a DNS of the NS equations. We examined the modification of the decaying isotropic turbulence by an enormous number of dumbbells (of the order of $O(10^{10})$) dispersed within the turbulence. We observed a significant energy dissipation reduction and energy spectrum modification in the later stages of decay when the concentration of polymers or the Weissenberg number was increased. These are entirely consistent with the results of DNSs using the constitutive equations (Perlekar *et al.* 2006; Cai *et al.* 2010). An interesting finding was the power-law decay of the kinetic energy spectrum, $E(k, t) \sim k^{-4.7}$, below the Kolmogorov length scale when $W_i = 25$. This power-law spectrum is due to the elastic nature of the ensemble of dumbbells. The spectrum was steeper than that inferred from the elastic turbulence. Thus, it is imperative to clarify the difference between the elastic turbulence and the present results by performing lower-R_λ and higher-W_i simulations than in the present study.

Investigation of the coherent vortices in terms of the second invariant Q of $\boldsymbol{\nabla u}$ found that the generation of intense vortices was suppressed by the polymer additives. This observation is consistent with the observed reduction in the energy dissipation rate. We also showed that regions containing extended dumbbells had sheet-like or filament-like structures, which were located among intense vortices. This implies that the stretched polymers tend to locate in the $Q < 0$ region, which is dominated by the strain. This is also consistent with the results of our previous study, in which the conditional mean distance of a polymer chain on Q and R had a large value in the region $Q < 0$, $R > 0$ (Watanabe & Gotoh 2010).

We found that the spectral tails were greatly affected by polymer additives, and the degree of modification was dependent on the parameters b and $\tilde{N}_t$, even though $N_t = b\tilde{N}_t$ was fixed. This nature was confirmed by examining the vortical structures, where it was found that as $\tilde{N}_t$ decreased, the surface of the vortices appeared to be rougher due to an insufficient convergence of $\boldsymbol{T}^p$ at grid scales.

The results obtained in this study indicate that the hybrid approach with parallel computation is an effective method for investigating dilute polymer solution flows. Although we used a simple dumbbell model for the long-chain polymer, it is interesting to introduce a more realistic polymer chain model that includes hydrodynamic interactions or excluded volume forces among beads (Doi & Edwards 1986). The hybrid approach is distinctly suited to examining the effect of these extra forces on turbulence modification, which has not been done in studies with constitutive equations, and will be the subject of a future work.

Acknowledgements

The authors thank R. Rubinstein, I. Fouxon and J. Schumacher for various comments. The work of T.W. and T.G. was partially supported by Grants-in-Aid for Scientific Research Nos. 20760112, 23760156, and 21360082, 24360068, respectively, from the Ministry of Education, Culture, Sports, Science, and Technology of Japan. T.W. thanks S. Uno and D. Sugimoto for their assistance in writing the parallelized code. The authors thank the Theory and Computer Simulation Centre of the National Institute for Fusion Science, and JHPCN and HPC at the Information Technology Centre of Nagoya University for providing the computational resources.

Appendix. Derivation of polymer stress tensor (2.10)

In this appendix, we derive the expression (2.10) for the polymer stress tensor from the fundamental equations of motion.

The equations of motion for the nth dumbbell are written as

$$\mathbf{0} = -\zeta(\dot{\boldsymbol{x}}_\alpha^{(n)} - \boldsymbol{u}(\boldsymbol{x}_\alpha^{(n)}, t)) + \boldsymbol{F}_\alpha^{(n)} + D\boldsymbol{W}_\alpha^{(n)} \tag{A 1}$$

where α indicates the label of the beads in the nth dumbbell ($\alpha = 1$ or 2). The elastic force of the dumbbell is defined by $\boldsymbol{F}_1^{(n)} = -kf(|\boldsymbol{x}_1^{(n)} - \boldsymbol{x}_2^{(n)}|/L_{max})(\boldsymbol{x}_1^{(n)} - \boldsymbol{x}_2^{(n)}) = -\boldsymbol{F}_2^{(n)}$ with $f(z) = (1 - z^2)^{-1}$ for the FENE model and the Stokes drag coefficient is $\zeta = 6\pi\nu_s a\rho_s$. We set the value of the constant to $D \equiv \sqrt{2\zeta k_B T}$. The random force $\boldsymbol{W}_\alpha^{(n)}$ obeys Gaussian statistics with a white-in-time correlation defined by (2.4) and (2.5).

The reaction force $\boldsymbol{A}$ to the fluid motion due to the ensemble of dumbbells is incorporated into the NS equations as

$$\frac{\partial \boldsymbol{u}}{\partial t} + \boldsymbol{u}\cdot\nabla\boldsymbol{u} = -\frac{1}{\rho_s}\nabla p + \nu_s\nabla^2\boldsymbol{u} + \frac{1}{\rho_s}\boldsymbol{A}, \tag{A 2}$$

where

$$\begin{aligned}\boldsymbol{A}(\boldsymbol{x}, t) &= -\sum_{n=1}^{N_t}[-\zeta(\boldsymbol{v}_1^{(n)} - \boldsymbol{u}(\boldsymbol{x}_1^{(n)}, t))\delta(\boldsymbol{x} - \boldsymbol{x}_1^{(n)}) - \zeta(\boldsymbol{v}_2^{(n)} - \boldsymbol{u}(\boldsymbol{x}_2^{(n)}, t))\delta(\boldsymbol{x} - \boldsymbol{x}_2^{(n)})] \\ &= \sum_{n=1}^{N_t}\boldsymbol{F}_1^{(n)}[\delta(\boldsymbol{x} - \boldsymbol{x}_1^{(n)}) - \delta(\boldsymbol{x} - \boldsymbol{x}_2^{(n)})] \\ &\quad + D\sum_{n=1}^{N_t}[\boldsymbol{W}_1^{(n)}\delta(\boldsymbol{x} - \boldsymbol{x}_1^{(n)}) + \boldsymbol{W}_2^{(n)}\delta(\boldsymbol{x} - \boldsymbol{x}_2^{(n)})].\end{aligned} \tag{A 3}$$

We also introduce the connector vector $\boldsymbol{R}^{(n)} = \boldsymbol{x}_1^{(n)} - \boldsymbol{x}_2^{(n)}$ and the centre of mass vector $\boldsymbol{r}_g^{(n)} = (\boldsymbol{x}_1^{(n)} + \boldsymbol{x}_2^{(n)})/2$. Then the delta function can be expressed by $\delta(\boldsymbol{x} - \boldsymbol{x}_1^{(n)}) = \delta(\boldsymbol{x} - \boldsymbol{r}_g^{(n)} - \boldsymbol{R}^{(n)}/2)$ and $\delta(\boldsymbol{x} - \boldsymbol{x}_2^{(n)}) = \delta(\boldsymbol{x} - \boldsymbol{r}_g^{(n)} + \boldsymbol{R}^{(n)}/2)$. If we introduce the notion of generalized function, we can expand $\delta(\boldsymbol{x} - \boldsymbol{r}_g^{(n)} \pm \boldsymbol{R}^{(n)}/2)$ as

$$\delta(\boldsymbol{x} - \boldsymbol{r}_g^{(n)} \pm \boldsymbol{R}^{(n)}/2) = \delta(\boldsymbol{x} - \boldsymbol{r}_g^{(n)}) \pm \frac{\boldsymbol{R}^{(n)}}{2}\cdot\nabla\delta(\boldsymbol{x} - \boldsymbol{r}_g^{(n)}) + O(|\boldsymbol{R}^{(n)}|^2). \tag{A 4}$$

By using the expansion (A 4) within $O(|\boldsymbol{R}^{(n)}|)$, (A 3) is approximated by

$$\begin{aligned}A_i(\boldsymbol{x}, t) &= -\frac{\partial}{\partial x_j}\sum_{n=1}^{N_t}\left\{F_{1i}^{(n)}R_j^{(n)} + \frac{D}{2}\delta w_i^{(n)}R_j^{(n)}\right\}\delta(\boldsymbol{x} - \boldsymbol{r}_g^{(n)}) \\ &\quad + 2D\sum_{n=1}^{N_t}w_{gi}^{(n)}\delta(\boldsymbol{x} - \boldsymbol{r}_g^{(n)})\end{aligned} \tag{A 5}$$

with $\boldsymbol{\delta w}^{(n)} \equiv \boldsymbol{W}_1^{(n)} - \boldsymbol{W}_2^{(n)}$ and $\boldsymbol{w}_g^{(n)} \equiv (\boldsymbol{W}_1^{(n)} + \boldsymbol{W}_2^{(n)})/2$. The third term of the RHS of (A 5) is expected to be zero when $N_t/L_{box}^3 \gg 1$ because the random force acting on the individual dumbbells at $\boldsymbol{x}$ is not correlated. Thus, we have

$$A_i(\boldsymbol{x}, t) = kr_{eq}^2\frac{\partial}{\partial x_j}\sum_{n=1}^{N_t}\left[\frac{R_i^{(n)}R_j^{(n)}}{r_{eq}^2}f\left(\frac{|\boldsymbol{R}^{(n)}|}{L_{max}}\right) - D\frac{\delta w_i^{(n)}R_j^{(n)}}{2k_BT}\right]\delta(\boldsymbol{x} - \boldsymbol{r}_g^{(n)}), \tag{A 6}$$

where $r_{eq} \equiv \sqrt{k_B T/k}$. The polymer stress tensor T^p_{ij} is defined by $A_i/\rho_s = \partial T^p_{ij}/\partial x_j$. Therefore, the stress tensor field due to the ensemble of dumbbells is given by

$$T^p_{ij}(\boldsymbol{x}, t) = \frac{\nu_s \eta}{\tau} \frac{L^3_{box}}{N_t} \sum_{n=1}^{N_t} \left[\frac{R^{(n)}_i R^{(n)}_j}{r^2_{eq}} f\left(\frac{|\boldsymbol{R}^{(n)}|}{L_{max}} \right) - D \frac{\delta w^{(n)}_i R^{(n)}_j}{2k_B T} \right] \delta(\boldsymbol{x} - \boldsymbol{r}^{(n)}_g), \tag{A 7}$$

where $kr^2_{eq} = (\rho_s \nu_s \eta/\tau)(L^3_{box}/N_t)$ with $\eta \equiv (3r_{eq}/4a)^2 \Phi_V$. Here Φ_V is the volume fraction of the ensemble of dumbbells and $\tau \equiv \zeta/4k$ is used.

We can further rewrite the second term of the RHS of (A 7). This term is expressed as

$$\frac{1}{N_t} \sum_{n=1}^{N_t} \delta w^{(n)}_i R^{(n)}_j \delta(\boldsymbol{x} - \boldsymbol{r}^{(n)}_g) = \langle \delta w^{(n)}_i R^{(n)}_j | \boldsymbol{x} \rangle_p \frac{1}{N_t} \sum_{n=1}^{N_t} \delta(\boldsymbol{x} - \boldsymbol{r}^{(n)}_g), \tag{A 8}$$

where the average with respect to the ensemble of dumbbells conditioned on $\boldsymbol{x}$ (ensemble member with the position vector $\boldsymbol{r}^{(n)}_g$ equal to $\boldsymbol{x}$) is defined by

$$\langle g^{(n)} | \boldsymbol{x} \rangle_p \equiv \frac{N_t^{-1} \sum_{n=1}^{N_t} g^{(n)} \delta(\boldsymbol{x} - \boldsymbol{r}^{(n)}_g)}{N_t^{-1} \sum_{n=1}^{N_t} \delta(\boldsymbol{x} - \boldsymbol{r}^{(n)}_g)}. \tag{A 9}$$

Because the interaction between different dumbbells is not considered in the present study, the above conditional average is approximated by the average over the realization of the random force such that

$$\langle \delta w^{(n)}_i R^{(n)}_j | \boldsymbol{x} \rangle_p \simeq \langle \delta w^{(n)}_i R^{(n)}_j \rangle \tag{A 10}$$

if the number of dumbbells located around $\boldsymbol{x}$ is large enough for the dumbbell statistics to sufficiently converge. Using the equation of motion for $\boldsymbol{R}^{(n)}$ (2.1) with conditions (2.4) and (2.5), it is straightforward to evaluate the RHS of (A 10). The result is $\langle \delta w^{(n)}_i(t) R^{(n)}_j(t) \rangle = D\delta_{ij}/\zeta$. We then arrive at the expression of the polymer stress tensor (2.10):

$$T^p_{ij}(\boldsymbol{x}, t) = \frac{\nu_s \eta}{\tau} \frac{L^3_{box}}{N_t} \sum_{n=1}^{N_t} \left[\frac{R^{(n)}_i R^{(n)}_j}{r^2_{eq}} f\left(\frac{|\boldsymbol{R}^{(n)}|}{L_{max}} \right) - \delta_{ij} \right] \delta(\boldsymbol{x} - \boldsymbol{r}^{(n)}_g). \tag{A 11}$$

REFERENCES

AFONSO, M. M. & VINCENZI, D. 2005 Nonlinear elastic polymers in random flow. *J. Fluid Mech.* **540**, 99–108.

ANGELIS, E. D. E., CASCIOLA, C. M., BENZI, R. & PIVA, R. 2005 Homogeneous isotropic turbulence in dilute polymers. *J. Fluid Mech.* **531**, 1–10.

ARRATIA, P. E., THOMAS, C. C., DIORIO, J. & GOLLUB, J. P. 2006 Elastic instabilities of polymer solutions in cross-channel flow. *Phys. Rev. Lett.* **96**, 144502.

BALKOVSKY, E., FOUXON, A. & LEBEDEV, V. 2000 Turbulent dynamics of polymer solutions. *Phys. Rev. Lett.* **84**, 4765–4768.

BERTI, S., BISTAGNINO, A., BOFFETTA, G., CELANI, A. & MUSACCHIO, S. 2006 Small-scale statistics of viscoelastic turbulence. *Europhys. Lett.* **76**, 63–69.

BERTI, S., BISTAGNINO, A., BOFFETTA, G., CELANI, A. & MUSACCHIO, S. 2008 Two-dimensional elastic turbulence. *Phys. Rev.* E **77**, 055306.

BIRD, R. B., CURTISS, C. F., AMSTRONG, R. C. & HASSAGER, O. 1987 *Dynamics of Polymetric Liquids, Vol. 2 Kinetic Theory*, 2nd edn. Wiley.

BOFFETTA, G., CELANI, A. & MAZZINO, A. 2005 Drag reduction in the turbulent kolmogorov flow. *Phys. Rev.* E **71**, 036307.

BOFFETTA, G., CELANI, A. & MUSACCHIO, S. 2003 Two-dimensional turbulence of dilute polymer solutions. *Phys. Rev. Lett.* **91**, 034501.

BOSSE, T., KLEISER, L. & MEIBURG, E. 2006 Small particles in homogeneous turbulence: Setting velocity enhancement by two-way coupling. *Phys. Fluids* **18**, 027102.

BRETHOUWER, G., HUNT, J. C. R. & NIEUWSTADT, F. T. M. 2003 Micro-structure and Lagrangian statistics of the scalar field with a mean gradient in isotropic turbulence. *J. Fluid Mech.* **474**, 193–225.

BURGHELEA, T., SEGRE, E. & STEINBERG, V. 2004 Mixing by polymers: Experimental test of decay regime of mixing. *Phys. Rev. Lett.* **92**, 164501.

BURGHELEA, T., SEGRE, E. & STEINBERG, V. 2006 Role of elastic stress in statistical and scaling properties of elastic turbulence. *Phys. Rev. Lett.* **96**, 214502.

BURGHELEA, T., SEGRE, E. & STEINBERG, V. 2007 Elastic turbulence in von Karman swirling flow between two disk. *Phys. Fluids* **19**, 053104.

CAI, W.-H., LI, D.-C. & ZHANG, H.-N. 2010 Dns study of decaying homogeneous isotropic turbulence with polymer additives. *J. Fluid Mech.* **665**, 334–356.

CELANI, A., MUSACCHIO, S. & VINCENZI, D. 2005*a* Polymer transport in random flow. *J. Stat. Phys.* **118**, 531–554.

CELANI, A., PULIAFITO, A. & TURITSYN, K. 2005*b* Polymers in linear shear flow: a numerical study. *Europhys. Lett.* **70**, 464–470.

CHERTKOV, M. 2000 Polymer stretching by turbulence. *Phys. Rev. Lett.* **84**, 4761–4764.

CHERTKOV, M., KOLOKOLOV, I., LEBEDEV, V. & TURITSYN, K. 2005 Polymer statistics in a random flow with mean shear. *J. Fluid Mech.* **531**, 251–260.

CHOI, H. J., LIM, S. T., LAI, PIK-YIN & CHAN, C. K. 2002 Turbulent drag reduction and degradation of DNA. *Phys. Rev. Lett.* **89**, 088302.

CRAWFORD, A. M., MORDANT, N., XU, H. & BODENSCHATZ, E. 2008 Fluid acceleration in the bulk of turbulent dilute polymer solutions. *New J. Phys.* **10**, 123015.

DAVOUDI, J. & SCHUMACHER, J. 2006 Stretching of polymers around the Kolmogorov scale in a turbulent shear flow. *Phys. Fluids* **18**, 025103.

DE GENNES, P. G. 1974 Coil–stretch transition of dilute flexible polymers under ultrahigh velocity gradients. *J. Chem. Phys.* **60**, 5030–5042.

DOI, M. & EDWARDS, S. F. 1986 *The Theory of Polymer Dynamics*. Oxford University Press.

ECKHARDT, B., KRONJAGER, J. & SCHUMACHER, J. 2002 Stretching of polymers in a turbulent enviroment. *Comput. Phys. Commun.* **147**, 538–543.

ELBING, B. R., DOWLING, D. R., PERLIN, M. & CECCIO, S. L. 2010 Diffusion of drag-reducing polymer solutions within a rough-walled turbulent boundary layer. *Phys. Fluids* **22**, 045102.

FOUXON, A. & LEBEDEV, V. 2003 Spectra of turbulence in dilute polymer solutions. *Phys. Fluids* **15**, 2060–2073.

FOUXON, I. & POSCH, H. A. 2012 Dynamics of threads and polymers in turbulence: power-law distributions and synchronization. *J. Stat. Mech.* P01022.

FRISCH, U. 1995 *Turbulence*. Cambridge University Press.

FUKAYAMA, D., OYAMADA, T., NAKANO, T., GOTOH, T. & YAMAMOTO, K. 2000 Longitudinal structure functions in decaying and forced turbulence. *J. Phys. Soc. Japan* **69**, 701–715.

GERASHCHENKO, S., CHEVALLARD, C. & STEINBERG, V. 2005 Single-polymer dynamics: coil–stretch transition in a random flow. *Europhys. Lett.* **71**, 221–227.

GERASHCHENKO, S. & STEINBERG, V. 2006 Statistics of tumbling of a single polymer molecule in shear flow. *Phys. Rev. Lett.* **96**, 038304.

GILLISSEN, J. J. J. 2008 Polymer flexibility and turbulent drag reduction. *Phys. Rev.* E **78**, 046311.

GOTOH, T. & WATANABE, T. 2012 Scalar flux in a uniform mean scalar gradient in homogeneous isotropic steady turbulence. *Physica* D **241**, 141–148.

GOTOH, T., WATANABE, Y., SHIGA, Y., NAKANO, T. & SUZUKI, E. 2007 Statistical properties of four-dimensional turbulence. *Phys. Rev.* E **75**, 016310.

GROISMAN, A. & STEINBERG, V. 2000 Elastic turbulence in a polymer solution flow. *Nature* **405**, 53–55.

GROISMAN, A. & STEINBERG, V. 2001 Efficient mixing at low Reynolds numbers using polymer additives. *Nature* **410**, 905–908.

JIN, S. & COLLINS, L. R. 2007 Dynamics of dissolved polymer chains in isotropic turbulence. *New J. Phys.* **9**, 360.

JUN, Y. & STEINBERG, V. 2009 Power and pressure fluctuations in elastic turbulence over a wide range of polymer concentrations. *Phys. Rev. Lett.* **102**, 124503.

LASO, M. & OTTINGER, H. C. 1993 Calculation of viscoelastic flow using molecular models: the Connffessit approach. *J. Non-Newtonian Fluid Mech.* **47**, 1–20.

LIBERZON, A., GUALA, M., KINZELBACH, W. & TSINOBER, A. 2006 On turbulent kinetic energy production and dissipation in dilute polymer solutions. *Phys. Fluids* **18**, 125101.

LIBERZON, A., GUALA, M., LÜTHI, B., KINZELBACH, W. & TSINOBER, A. 2005 Turbulence in dilute polymer solutions. *Phys. Fluids* **17**, 031707.

LIU, Y. & STEINBERG, V. 2010 Stretching of polymer in a random flow: effect of a shear rate. *Europhys. Lett.* **90**, 44005.

LUMLEY, J. L. 1973 Drag reduction in turbulent flow by polymer additives. *J. Polym. Sci.: Macromol. Rev.* **7**, 263–290.

MCCOMB, W. D., ALLAN, J. & GREATED, C. A. 1977 Effect of polymer additives on the small-scale structure of grid-generated turbulence. *Phys. Fluids* **20**, 873–879.

OUELLETTE, N. T., XU, H. & BODENSCHATZ, E. 2009 Bulk turbulence in dilute polymer solutions. *J. Fluid Mech.* **629**, 375–385.

PERLEKAR, P., MITRA, D. & PANDIT, R. 2006 Manifestations of drag reduction by polmer additives in decaying, homogeneous, isotropic turbulence. *Phys. Rev. Lett.* **97**, 264501.

PERLEKAR, P., MITRA, D. & PANDIT, R. 2010 Direct numerical simulations of statistically steady, homobeneous, isotropic turbulence with polymer additives. *Phys. Rev.* E **82**, 066313.

PETERS, T. & SCHUMACHER, J. 2007 Two-way coupling of finitely extensible nonlinear elastic dumbbells with a turbulent shear flow. *Phys. Fluids* **19**, 065109.

PROCCACIA, I., L'VOV, V. S. & BENZI, R. 2008 Theory of drag reduction by polymers in wall-bounded turbulence. *Rev. Mod. Phys.* **80**, 225–247.

PROSPERETTI, A. & TRYGGVASON, G. 2007 *Computational Methods for Multiphase Flow* (ed. A. Prosperetti & G. Tryggvason). Cambridge University Press.

SCHUMACHER, J., SREENIVASAN, K. R. & YEUNG, P. K. 2005 Very fine structures in scalar mixing. *J. Fluid Mech.* **531**, 113–122.

SREENIVASAN, K. R. & WHITE, C. M. 2000 The onset of drag reduction by dilute polymer additives, and the maximum drag reduction asymptote. *J. Fluid Mech.* **409**, 149–164.

STONE, P. A. & GRAHAM, D. 2003 Polymer dynamics in a model of the turbulent buffer layer. *Phys. Fluids* **15**, 1247–1256.

SURESHKUMAR, R., BERIS, A. N. & HANDLER, R. A. 1997 Direct numerical simulation of the turbulent channel flow of a polymer solution. *Phys. Fluids* **9**, 743–755.

TAMANO, S., ITOH, M., HOTTA, S., YOKOTA, K. & MORINISHI, Y. 2009 Effect of rheorogical properties on drag reduction in turbulent boundary layer flow. *Phys. Fluids* **21**, 055101.

TENNEKES, H. & LUMLEY, J. L. 1972 *A First Course in Turbulence*. MIT.

TERRAPON, V. E., DUBIEF, Y., MOIN, P., SHAQFEH, E. S. G. & LELE, S. K. 2004 Simulated polymer stretch in a turbulent flow using brownian dynamics. *J. Fluid Mech.* **504**, 61–71.

THIFFEAULT, J-L. 2003 Finite extension of polymers in turbulent flow. *Phys. Lett. A* **308**, 445–450.

VAITHIANATHAN, T. & COLLINS, L. R. 2003 Numerical approach to simulating turbulent flow of a viscoelastic polymer solution. *J. Comput. Phys.* **187**, 1–21.

VAN DOORN, E., WHITE, C. M. & SREENIVASAN, K. R. 1999 The decay of grid turbulence in polymer and surfactant solutions. *Phys. Fluids* **11**, 2387–2393.

WATANABE, T. & GOTOH, T. 2007 Inertial range intermittency and accuracy of direct numerical simulation of turbulence and passive scalar turbulence. *J. Fluid Mech.* **590**, 117–146.

WATANABE, T. & GOTOH, T. 2010 Coil–stretch transition in an ensemble of polymers in isotropic turbulence. *Phys. Rev.* E **81**, 066301.

YASUDA, S. & YAMAMOTO, R. 2010 Multiscale modelling and simulation for polymer melt flows between parallel plate. *Phys. Rev.* E **81**, 036308.

YEUNG, P. K. & POPE, S. B. 1988 An algorithm for tracking fluid particles in numerical simulations of homogeneous turbulence. *J. Comput. Phys* **79**, 373–416.